McKelvey School of Engineering Theses & Dissertations

McKelvey School of Engineering

Spring 5-15-2017

Using PET/MRI to Assess Hepatic Radioembolization of Yttrium-90 Microspheres

Nichole Millward Maughan
Washington University in St. Louis

Follow this and additional works at: https://openscholarship.wustl.edu/eng_etds

Part of the Biomedical Commons

WASHINGTON UNIVERSITY IN ST. LOUIS

School of Engineering and Applied Science

Department of Biomedical Engineering

Dissertation Examination Committee:
Parag Parikh, Chair
Mark Anastasio
Hong Chen
Harold Li
Richard Wahl
Pamela Woodard

Using PET/MRI to Assess Hepatic Radioembolization of Yttrium-90 Microspheres

by

Nichole Millward Maughan, M.S.

A dissertation presented to
The Graduate School
of Washington University in
partial fulfillment of the
requirements for the degree
of Doctor of Philosophy

May 2017
Saint Louis, Missouri

Contents

List of Figures

List of Tables

Acknowledgments

First, I would like to thank my principal investigator, Dr. Parag Parikh, for his incredible amount of support and mentorship, both professionally and personally. He afforded me more opportunities than I could even imagine to develop my professional skills and pursue my endeavors. He pushed me to reach higher than I ever thought I could and always had my back. I am so thankful for the opportunities he gave me to work with so many incredible people on such a rewarding project.

I would also like to thank Dr. Richard Laforest for serving as a second research advisor to me. Without him, I could not have performed any of the phantom experiments. He was instrumental in the design and implementation of the phantom experiments and was my go-to person for all things technical.

I would also like to thank Dr. Kathryn Fowler for her support with the clinical studies, dedicating so much time to drawing and approving contours, as well as including me as a co-first author on our manuscript.

I would also like to thank the members of my committee, Drs. Mark Anastasio, Hong Chen, Harold Li, Richard Wahl, and Pamela Woodard, for their support and insight.

I would also like to thank the many others who supported me: Drs. Maurizio Conti and David Faul from Siemens Healthcare for insight and research support with phantom studies; Michael Tapner from Sirtex for funds to travel to several conferences and to perform the

Dedicated to my dear uncle, Larry Millward.

ABSTRACT OF THE DISSERTATION

Using PET/MRI to Assess Hepatic Radioembolization of Yttrium-90 Microspheres

by

Nichole Millward Maughan

Doctor of Philosophy in Biomedical Engineering

Washington University in St. Louis, May 2017

Research Advisor: Dr. Parag Parikh, M.D., B.S.E.

Radioembolization of yttrium-90 (^{90}Y) microspheres is used to treat primary and secondary cancers in the liver. Though this therapy has existed for decades, the treatment is not well optimized from treatment planning to post-procedural assessment. Recently, there has been a surge to utilize the small positron yield from the radioactive decay of ^{90}Y for post-radioembolization positron emission tomography (PET) imaging of the microsphere activity distribution. These images provide promise for dosimetry assessment, identifying extra-hepatic uptake and possible under-dosed lesions that may benefit from subsequent therapy. However, due to the low positron statistics and high flux of Bremsstrahlung radiation, PET imaging of ^{90}Y presents with its own unique set of challenges. In this work, we optimized the PET imaging acquisition and reconstruction parameters when imaging with a hybrid PET/MRI scanner to offer the most accurate images for quantitative dosimetric applications. We then tested the variability of imaging ^{90}Y with PET across multiple institutions in a world-wide phantom study in preparation for a multi-institutional phase I/II clinical

trial. Lastly, we determined the clinical utility of using ^{90}Y PET-based dosimetry to predict clinical outcomes and assess how well it correlates with pre-treatment imaging.

Chapter 1

Introduction

1.1 Background

1.1.1 Cancer in the Liver

Primary liver cancers, such as hepatocellular carcinoma (HCC) and cholangiocarcinoma (CAA), are the tenth most common form of cancer and the fifth and ninth most common cause of cancer death of men and women, respectively [1]. Survival rates for those with primary liver disease are low, with the 1-year survival rate being 43% and the 5-year survival rate being 17%. Even with an early diagnosis, the 5-year survival rate is only 30%. For late stages of liver cancer, survival rate decreases to as low as 3% [2].

More common than primary liver cancer are tumor metastases to the liver, with the most common types of metastases being lung, breast, and colorectal cancer (mCRC) [3]. Both the dual blood supply to the liver, i.e. the hepatic artery and portal vein, and the easy penetration through the hepatic sinusoids, characteristic to the function of the liver, allow for the high incidence rate of hepatic metastases [3].

Colorectal carcinoma is the third most common malignancy and third most common cause of cancer-related mortality in the United States. Over one-half of patients with mCRC develop hepatic metastatic disease; and one-third have hepatic metastases present at diagnosis [4]. Prognosis is very dependent on the development of liver metastases.

There are several methods for treating cancer in the liver, including surgical removal of the tumor or affected lobe, radiofrequency ablation, chemotherapy, and/or radiation [5]. Many patients are not diagnosed until the disease has developed significantly, making them incompatible for surgical intervention [6]. For these patients, other modes of treatment such as radiation therapy may be the best course of treatment.

There are two main types of radiation therapy: external beam, where a high energy beam of photons, electrons, or protons is directed towards the regions of the tumors, and brachytherapy, where sealed radioactive sources are implanted in the patient near or in the tumors. In the case of the liver, healthy liver tissue has a lower tolerance to radiation than the cancerous tissue, and when too much healthy liver is exposed to radiation, there is a greater possibility of radiation–induced liver disease (RILD), including liver dysfunction [7].

1.1.2 Yttrium-90 Radioembolization

A palliative form of therapy for primary and metastatic disease in the liver is brachytherapy using the beta-emitter yttrium-90 (^{90}Y, 64.1 hr half-life; 0.93 MeV β-emission; tissue penetration mean 2.5 mm, maximum 11 mm) as the radioactive source. Yttrium-90 radioembolization, which involves intra-arterial delivery of radioactive microspheres to the tumors, is often used for patients with cancer in the liver who are not candidates for surgery. Physicians can utilize the angiogenesis of liver tumors as well as the physiology of the liver to selectively

deliver ^{90}Y microspheres to the tumors. Liver tumors receive most of their blood supply from the hepatic artery [6, 7] while the liver itself receives about 75% of its blood supply from the portal vein with the other 25% being from the hepatic artery [8]. The physician injects the microspheres into the hepatic artery via catheterization, and, ideally, the spheres will localize and deposit in the tumors. This allows the tumors to be exposed to radiation while sparing the healthy liver.

Developed in the late 1990s, the use of radioembolization has been quickly increasing, with over 15,000 administrations delivered last year. There have been many institutional reports on effectiveness in both primary and metastatic liver cancer [9–11]. Large, prospective trials on radioembolization are underway in HCC and mCRC. Recently, there was a phase III randomized study comparing chemotherapy with or without radioembolization in patients with liver-only mCRC [12]. In this study, there was an improvement in complete response of liver metastases, as well as a median 7.9 month improvement in time to liver progression.

TheraSpheres and SIR-Spheres are the two brands of ^{90}Y microspheres available on the market today for hepatic radioembolization [6]. Specifications about these microspheres are given in Table 1.1. TheraSpheres are typically used for treatment of HCC and pancreatic neuroendocrine carcinoma metastases (mNET) while SIR-Spheres are used typically used for metastases, such as mCRC and mNET.

Name	Manufacturer	Material	Diameter (μm)	Specific Activity (Bq/sphere)
Theraspheres	Nordion (Ottawa, Canada)	Glass	20-30	2500
SIR-Spheres	Sirtex (Sydney, Australia)	Resin	35	50

Table 1.1: ^{90}Y microsphere specifications by brand

1.1.3 Lack of Radioembolization Dosimetry

There is an established planning and dosing method for radioembolization that is predicated on patient safety (see Figure 1.1). First, patients have an angiogram of the hepatic artery system. The angiogram is used to investigate variant vascular anatomy and to embolize branches that would lead to non-target (such as gastrointestinal tract) embolization. When the interventional radiologist feels confident that all non-target vascular flow has been embolized, he/she will place the catheter in the planned location (often the right or left hepatic artery) and inject Technetium-99m macroaggregated albumin (^{99m}Tc-MAA). The patient will then go to nuclear medicine for a SPECT scan, and this scan will be evaluated for 1) low shunt of particles to the lung and 2) no gastrointestinal tract uptake. If these safety criteria are met, the patient becomes a candidate for transcatheter ^{90}Y microsphere treatment. The amount of ^{90}Y activity ordered differs between the two microsphere manufacturers, based on their original safety data (see Figure 1). The patient is then scheduled for treatment where the interventional radiologist attempts to place the catheter in the exact same place as during the planning angiogram, and, assuming comparable vascular blood

4

flow and hemodynamics as on the day of treatment planning, delivers the ^{90}Y microspheres. Another assumption is that the ^{90}Y microspheres are delivered uniformly throughout the region or volume supplied by the selected vessel (lobar, segmental, or subsegmental). However, based on anecdotal observations and small case studies, variability of lesion response on subsequent imaging exams implies an inhomogeneous microsphere distribution and variable radiation dose to the treated lesion(s) [13].
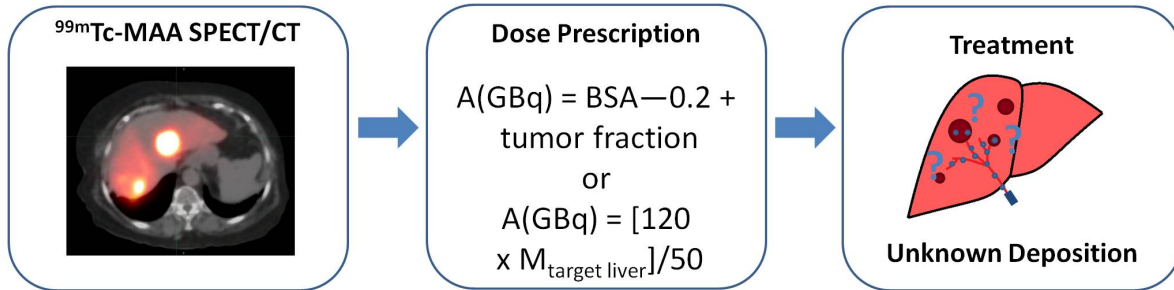
Figure 1.1: Flow-chart for the planning and administration of ^{90}Y microspheres for hepatic radioembolization. The current workflow for radioembolization requires waiting 3-6 months for follow-up imaging to assess treatment efficacy.

Activity delivered to patients typically ranges from 3–20 GBq per delivery for glass microspheres and typically 2 GBq per delivery for resin microspheres [14]. Prescribed activity for Theraspheres (glass), which are typically delivered to patients with HCC or mNET, is determined by the following equation recommended by the manufacturer:

$$A(\text{GBq}) = [D_{\text{desired}}(\text{Gy}) \times M_{\text{target liver}}(\text{kg})]/50 \qquad (1.1)$$

Note that Eq. 1.1 is independent of tumor burden. Prescribed activity for SIR-Spheres (resin), which are typically delivered to patients with metastatic lesions to the liver (e.g. mCRC and mNET), is determined either via the body surface area method:

$$A(\text{GBq}) = \text{BSA} - 0.2 + (\%\text{tumor involvement}/100) \tag{1.2}$$

or by utilizing the percentage of tumor burden on the liver:

$$< 50\% \rightarrow 3.0\text{GBq} \tag{1.3}$$

$$25 - 50\% \rightarrow 2.5\text{GBq} \tag{1.4}$$

$$< 25\% \rightarrow 2.0\text{GBq} \tag{1.5}$$

The above prescribed activities are reduced if the lung shunt fraction, determined from the ^{99m}Tc-MAA SPECT, is above 10-20%. A significant limitation in these equations is the assumption that the delivered dose will distribute uniformly throughout the target region.

Ho *et al.* and Campbell *et al.* have proposed using the pre-treatment MAA SPECT to predict the efficacy of radioembolization before the microspheres are delivered [15, 16]. However, this method assumes that the MAA particles are delivered in the same manner as the ^{90}Y microspheres despite the difference in sizes of the particles (10–150 μm and 20–35 μm for MAA and ^{90}Y microspheres, respectively) and difference in days of delivery, which results in different catheter placements [17, 18].

There is a growing interest in post-delivery imaging of these ^{90}Y microspheres to make assessments of possible extra-hepatic deposition and toxicity as well as assessing tumor coverage in order to predict response as early as possible [18–23]. Currently, there is no standard for post-delivery imaging of ^{90}Y.

1.1.4 Benefits of Lesion Specific Dosimetry

The role of regional hepatic therapy to downstage a patient for surgery has been well described. Patients who are downstaged to resection from regional liver therapy have significantly improved survival, with one study showing a 49% 5-year survival versus 3% 5-year survival for those who could not receive surgery [24]. Early lesion specific outcome could move patients from the non-surgery arm to one with surgery or to other local ablative therapies such as radiofrequency ablation, microwave ablation, cryoablation, irreversible electroporation or stereotactic radiation.

Unfortunately, the radiographic response by CT and MRI to radioembolization therapy is difficult to interpret at 3 months, and often one has to wait 6 months for resolution of treatment related liver changes. A recent study by Kennedy et al. [25] investigated the radiographic response in 9 centers using pre-treatment imaging within 3 months of therapy and follow-up therapy at 90 days. They found that the 3 month response rate underrepresented maximal response by 5-10%, with over half the patients with confounding factors such as peritumoral edema and necrosis. Findings such as these may delay subsequent therapies.

In conclusion, existing methods of evaluating dose in radioembolization suffer from poor spatial resolution, inability to delineate the lesions of interest, unclear relationships between planning and delivery, and low patient numbers in evaluations of dose relating to outcomes.

1.2 Innovation

1.2.1 Post-Implant Dosimetry in Interventional Radiology

Post-implant dosimetry is a standard procedure with other forms of brachytherapy, such as low-dose prostate brachytherapy. The clinical work-flow for low-dose prostate therapy involves obtaining planning images of the prostate, then the operator implants radioactive seeds with image guidance. This work-flow used to be considered sufficient, but further research found that post-implant dosimetry, which involves identifying the seed location and prostate boundary with a post-procedural CT, is crucial for tumor control [26]. Recently, there were reports of toxicities and poor outcomes at a VA facility that didn't use post-implant dosimetry for their patients [27]. Due to these events, post-implant dosimetry is now routine [28].

Unfortunately, there is little infrastructure available to the interventional radiologist or nuclear medicine physician, to perform this analysis in current clinical workflow. We propose a new workflow, where the patient can have immediate post-treatment evaluation and then have lesion specific measurements of response.

Post-radioembolization imaging has been proposed with Bremsstrahlung SPECT/CT from the β- decay of ^{90}Y [23, 29–31]. Bremsstrahlung SPECT, however, offers low-resolution images that can often fail to identify uptake in small lesions, areas of tumor thrombus, and extra-hepatic uptake [19].

^{90}Y decays predominantly by β- decay to the ground state of ^{90}Zr with a weak transition to the 1.76 MeV 0+ (0.0115%) excited state. Gamma decay of this level is strictly forbidden since the ^{90}Zr ground state is also 0+ [21]. This level will decay by electron conversion

with a small decay branching fraction by internal pair production ($\beta+/\beta-$ emission) [21, 32]. The positrons emitted during this decay process, although few (∼32 ppm), allow for imaging of ^{90}Y activity via positron emission tomography (PET) [32]. The kinetic energy spectra of the positrons can be described from energy-momentum analysis and is predicted to have a maximum energy of 738 KeV and average energy of 369 KeV. These values are commensurate to the positrons emitted from ^{18}F and therefore similar loss of resolution from the positron range is expected [33]. Furthermore, with simultaneous imaging of PET and an anatomic imaging modality such as CT or MRI, one can more precisely measure where the ^{90}Y microspheres are localizing, whether healthy liver, cancerous, or extrahepatic tissues.

Previous groups have reported using PET/CT for post-radioembolization ^{90}Y imaging. [20, 32, 34–37], as these scanners are more common and readily available. However, CT exposes the patient to additional, unnecessary ionizing radiation. MRI, on the other hand, does not utilize ionizing radiation, plus, it offers excellent soft-tissue contrast [38] that CT is not capable of, allowing us to more clearly see the boundaries of the liver lesions. Thus, we are interested in determining how useful PET/MRI would be with assessing the distribution of ^{90}Y microspheres following delivery. In the process, we are also interested in obtaining a quantitative assessment of the microsphere delivery using PET/MRI.

1.2.2   Application of PET/MRI in Radioembolization Dosimetry

The PET/MR is uniquely positioned to solve the underlying problems with radiation dosimetry. Compared to CT, MRI offers excellent soft-tissue contrast (see Figure 1.2), which is essential for accurately delineating healthy liver tissue versus tumors during analysis [38]. Many

have found that although contrast-enhanced MRI and contrast-enhanced CT have comparable sensitivities with detecting large liver lesions, MRI has a much higher sensitivity with detecting small liver lesions [39–41], which are common among patients with metastatic disease. Furthermore, contrast-enhanced imaging, especially CT, is contraindicated in patients with poor renal function. When contrast-enhanced imaging is not an option, unenhanced MRI is superior to unenhanced CT in the detection and characterization of lesions in the liver [42]. Thus, there is a growing interest in using the newly developed hybrid PET/MRI scanners where high quality anatomical information from the MRI and localization information about the microspheres from PET together have potential for improving patient care by predicting clinical outcomes for ^{90}Y radioembolization immediately after delivery. Predicting clinical outcomes immediately after radioembolization rather than waiting for follow-up imaging, typically 3 months after the procedure, could guide additional therapy for patients much sooner than what is currently done in the clinic today.
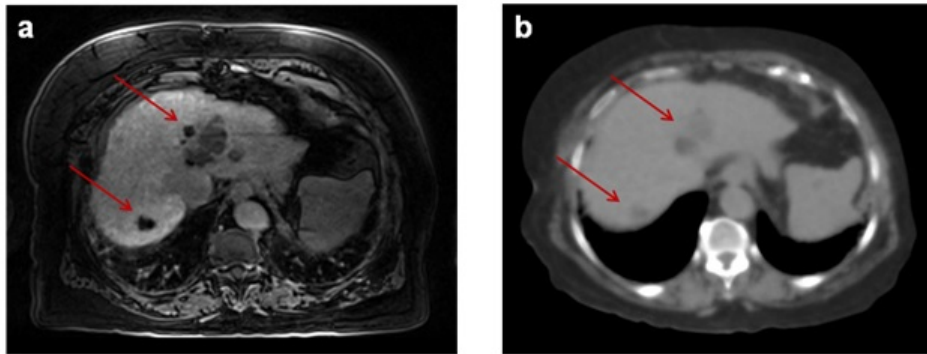
Figure 1.2: (a) MRI versus (b) CT of patient with primary liver cancer. The lesions, indicated by the red arrows, and their boundaries are much clearer on the MRI compared to the CT.

The PET/MR being used in the study also has the advantage of simultaneous acquisition of PET and MR images. This allows better fusion of images versus those acquired at disparate times, as well as the opportunity to allow for motion correction of the PET images. Given

the low counts when measuring ^{90}Y with PET, this has the potential for improvement of lesion quantification [43].

The aims of this work are three-fold:

Aim 1: We will maximize the signal to noise ratio of yttrium-90 PET by optimizing acquisition and reconstruction parameters for yttrium-90 PET/MR, performed on a commercially available, fully-integrated PET/MRI unit.

Aim 2: We will test the reproducibility of imaging yttrium-90 on PET/MRI to establish the reliability of yttrium-90 PET dosimetry.

Aim 3: We will use dose calculated from post-radioembolization PET/MRI to determine a dosimetric quantity that can be used for predicting individual lesion response.

Chapter 2

Optimal PET reconstruction parameters for imaging ^{90}Y on PET/MRI †

2.1   Introduction

Significant differences between the PET cameras on PET/CT and the Siemens Biograph mMR PET/MRI evoke the need for determining optimal PET reconstruction parameters when imaging ^{90}Y on the mMR. These differences include the use of avalanche photodiode (APD) detectors instead of photomultiplier tubes (PMT); the smaller detector block size; more crystals; the longer axial field of view (FOV); reduced crystal ring diameter; and the longer coincidence timing window as compared to the counterpart PET/CT scanners

---

†This chapter has been previously published in [44]. https://doi.org/10.1088/2057-1976/2/1/015009 © IOP Publishing. Reproduced with permission. All rights reserved

In this study, we aim to find optimal ^{90}Y-PET reconstruction parameters for a hybrid PET/MRI scanner. We investigate the effects of using various combinations of reconstruction parameters, including with and without PSF, and different scatter correction methods. We also investigate the effects of scan time duration. To our knowledge, although there have been many investigations involving ^{90}Y PET/CT, no other validation work has been published for ^{90}Y-PET in PET/MRI cameras.

2.2   Materials and Methods

2.2.1   Phantom Preparation

Nearly 8 GBq of ^{90}Y chloride solution was used for filling the standard ACR phantom. Although microspheres are used for patient treatment, we used solution to avoid the issue of settling. Solution used for filling of the hot cylinders was measured and diluted such that there would be an initial activity concentration of 13.1 MBq/mL in the hot cylinders and a 10:1 activity concentration ratio between hot cylinders and the warm background. A similar ratio of 8:1 was used in the large-scale ^{90}Y PET/CT QUEST study [37]. The activity concentration ratio between tumor and the treated side of the liver in patients is typically 2:1 while the ratio between tumor and background (paraspinal region) is typically 85:1. Cylinders of 8, 12, 16, and 25 mm diameters were filled with the hot activity. One of the other three 25 mm diameter cylinders was filled with cold water (no activity), one was left empty with air, and the third was a solid plastic cylinder (see Figure 2.1).
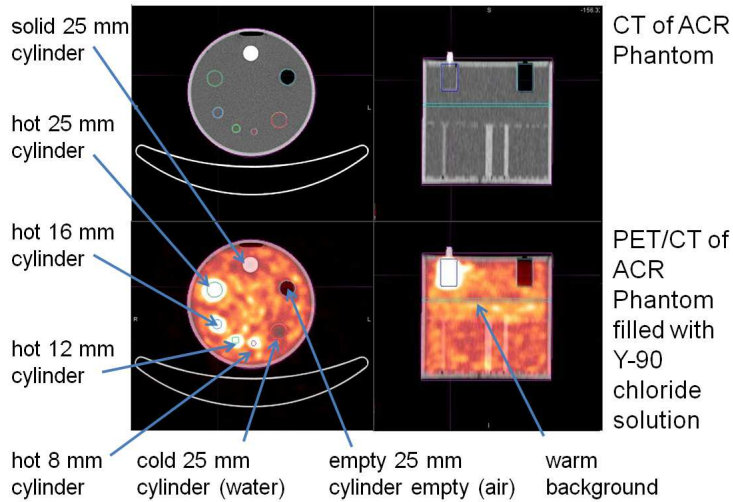
Figure 2.1: CT (top) and fused PET and CT images (bottom) of ACR phantom filled with ^{90}Y.

2.2.2 Data Acquisition

In this study, we used the Siemens Biograph mMR scanner at two separate institutions (Washington University in St. Louis, MO and Icahn School of Medicine at Mount Sinai, New York, NY). The PET portion of the scanner consists of 8 rings of 56 detector blocks each composed of an array of 8x8 of 4x4x20 mm LSO scintillation crystals with 9 avalanche photodiodes (APD) per block and a 5.86 ns coincidence window timing window.

MR-based attenuation correction on the mMR is typically done using segmentation methods on a 2-point Dixon sequence. The acquired in-phase and out-of-phase water and fat images are processed to create a segmented attenuation map that is separated into four tissue classes: background, lungs, fat, and soft tissue [45]. Although water in the ACR phantom can be seen well in MR images, the plastic casing and MR hardware (e.g. RF coils) cannot. Both the plastic and hardware provide significant attenuation and need to be included for accurate

PET measurements [46]. PET/MR attenuation correction of the phantom was provided by a CT scan scaled to the PET attenuation coefficient [47]. CT images of the body phased array MR coil were similarly processed and registered to the MR-Dixon water image using fiducial markers and then added to the phantom attenuation maps. The couch attenuation map is included as fixed hardware attenuation map in the image reconstruction process.

The phantom was imaged in listmode for 30 minutes per scan. The phantom was placed at the center of the FOV, aligned along the long axis of the scanner using the positioning laser. Scans were obtained at six total activity levels between 7.43 GBq and 1 GBq where the phantom was left to decay to the six different activity time points (see Table 2.1).

Table 2.1: Total activity in phantom at time of acquisition for each of the six scans at each institution.

	Washington University in St. Louis (GBq)	Icahn School of Medicine at Mount Sinai (GBq)
Scan 1	7.42	7.43
Scan 2	6.22	6.48
Scan 3	5.75	5.58
Scan 4	4.42	4.55
Scan 5	2.20	1.97
Scan 6	1.00	1.06

2.2.3 Count Rates

We investigated the possible loss of counts at high activity by recording Singles, True coincidences and delayed coincidences (Randoms) during exposure for all scans. Count rates were extracted both from the console and the sinogram headers.

2.2.4 Image Reconstructions and Analysis

All images were generated using the e7tools suite of image reconstruction software, an offline reconstruction tool provided by Siemens that allows more flexibility, more debugging information, and easier handling of large reconstruction queues than the mMR scanner console (Siemens, Knoxville, TN). The implementation of the reconstruction algorithms is the same in both e7tool suite and mMR console, since both execute calls to the same low level reconstruction routines. Listmode data were sorted as 3-dimensional (3D) sinograms with separate Prompts and Randoms with Random smoothing in the image reconstruction process. PET images were reconstructed with the 3D ordinary Poisson ordered subset expectation maximization (OP-OSEM) algorithm using combinations of the following reconstruction parameters: 1 to 5 iterations; 21 subsets (default on mMR); 5 mm and 10 mm Gaussian post-reconstruction filter; with and without point spread function (PSF, no PSF); and absolute and relative scatter scaling correction.

Two scatter correction methods are available on the Siemens PET/CT or PET/MR cameras: the absolute scatter correction, which is based solely on the amount of activity in the FOV and the attenuation map, and the relative scatter correction, which scales the absolute scatter correction to the tail of the counts measured outside the phantom. The single scatter simulation (Watson 2000) provides an estimate of the scatter distribution in the presence

of activity within a defined attenuation map. The scatter distribution can be calculated in an absolute amount if the activity concentration in the object is known and the attenuation map is accurately measured based on the well-known Klein-Nishina equation and electron density in the media. The limitation of this approach is that if activity is located outside the axial FOV, the scatter distribution will be underestimated. Thus a relative scatter correction is available from which the scatter distribution is scaled in order to match the sinogram tails outside the patient or the object being imaged (Watson 2000). This method is particularly useful for whole-body scans where some of the activity might be outside the axial FOV. Because the ^{90}Y PET data is noisy, we tested both scatter correction approaches to determine which method provides minimum bias of measured activity.

A second set of reconstructions was performed using the first 15 minutes of listmode data to compare the effects of reduced scan time

All analyses were performed on either MIMVista (MIM Software, Cleveland, OH) or in MATLAB (Mathworks, Natick, MA). Regions of interest (ROIs) were drawn for each cylinder as delineated on the CT images of the phantom, in both height and diameter (see Figure 2.1). Each PET scan was then registered to the CT image, and the ROIs statistics were extracted from each PET scan. The ROIs included one for each of the differently sized hot cylinders, one for the entire phantom, and one exclusively for a portion (151.5 mL) of the warm uniform background, as shown in Figure 2.1.

The coefficient of variation (COV) in the warm background, was calculated for each scan using

$$COV = \frac{\sigma_{background}}{\mu_{background}} \tag{2.1}$$

where $\sigma_{background}$ and $\mu_{background}$ are the standard deviation and average activity of a ROI within the warm background region of the phantom, respectively (see Figure 2.1).

Recovery coefficients (RCs) were calculated as

$$RC_i = \frac{A_i^{measured}}{A_i^{true}} \tag{2.2}$$

where RC_i is the recovery coefficient for a specific ROI i, $A_i^{measured}$ is the measured total activity in ROI i, and A_i^{true} is the expected total activity in ROI i. A value of 1 indicates that the measured amount of activity equals the true amount of activity.

We evaluated the relative change in RC from the PSF reconstructions relative to the no PSF reconstruction at two iterations using the formula:

$$\Delta_{RC}(\%) = \frac{RC_i^{PSF} - RC_2^{noPSF}}{RC_2^{noPSF}} \times 100 \tag{2.3}$$

and the relative change in coefficient of variation using:

$$\Delta_{COV}(\%) = \frac{COV_i^{PSF} - COV_2^{noPSF}}{COV_2^{noPSF}} \times 100 \tag{2.4}$$

where RC_2^{noPSF} and COV_2^{noPSF} are the recovery coefficients and coefficient of variation of the warm background, respectively, for reconstructions with 2 iterations and no use of PSF, and RC_i^{PSF} and COV_i^{PSF} are the recovery coefficients and coefficient of variation of the warm background, respectively, for reconstructions with i iterations and use of PSF.

2.3 Results

2.3.1 Count Rates

The recorded *Singles*, *Randoms*, and *Trues* rates from the emission sinogram are presented in Figure 2.2. Plots are *Singles* rate per block, total *Randoms* rate in the scanner and total *Trues* rate in the scanner as a function of activity. Both the *Singles* and *Trues* rates are linear with increasing activity ($R^2 = 0.9981$ and 0.9919, respectively), while the *Randoms* rates are quadratic with activity ($R^2 = 0.9993$).
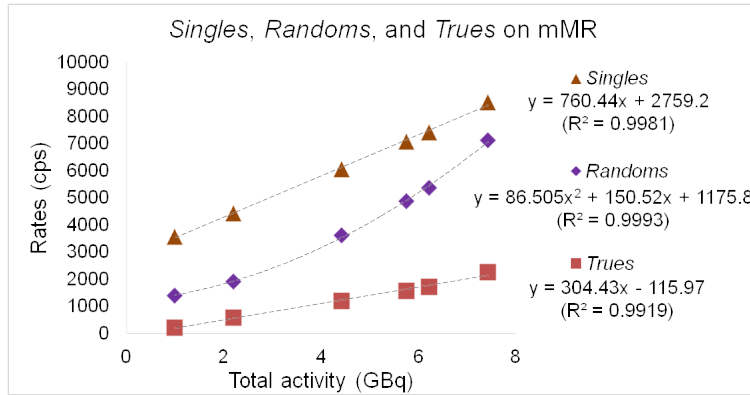
Figure 2.2: Singles, Randoms, and Trues count rates measured from the sinogram headers for the mMR when imaging ^{90}Y. Fitted curves to data points are shown as dashed lines.

Measured activity in the entire phantom for several reconstructions is compared to the expected activity in Figure 2.3 along with the identity line (dashed). We observed a linear relationship with increasing activity. Reconstructions with relative scatter correction exhibited a positive bias while reconstructions utilizing absolute scatter correction exhibited a negative bias.
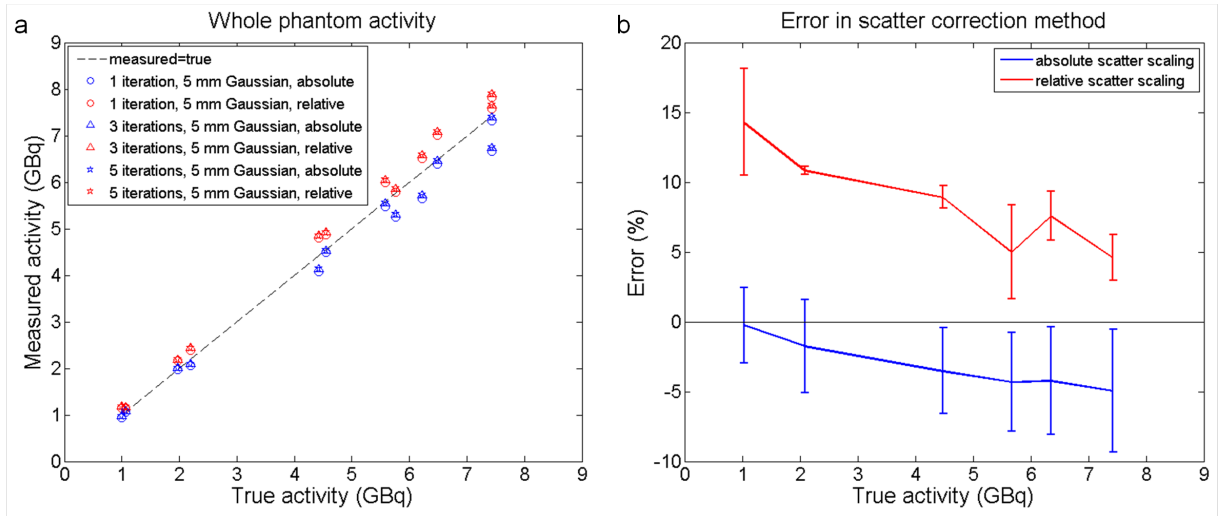
Figure 2.3: (a) Measured activity versus expected activity in entire phantom from reconstructed PET images with 1, 3, or 5 iterations, a 5 mm Gaussian post-reconstruction filter, and either absolute or relative scatter scaling correction. (b) Difference between measured versus true activity in the entire phantom for two different scatter scaling methods, relative (red) and absolute (blue) (3 iterations, 21 subsets, 5 mm Gaussian, PSF). Error bars represent the range of values between the institutions.

2.3.2 Scatter Correction Method

Figure 2.3b compares the results from using either relative or absolute scatter scaling during image reconstruction. Relative scatter scaling reconstructions slightly overestimated the activity in the phantom while absolute scatter scaling reconstructions tended to underestimate the activity in the phantom at high activities. Absolute scatter scaling offered the least amount of variability from the true total activity amount (within 10%), even though it consistently slightly underestimated the activity.

2.3.3 Optimal Reconstruction Parameters without PSF

Figure 2.4 shows the RC plotted against noise for all non-PSF reconstructions for each of the four hot cylinders for all six total activity levels. Reconstructions with the 10 mm Gaussian post-reconstruction filter had much lower RCs than all reconstructions with the 5 mm Gaussian filter, with the exception of the 1 iteration, 5 mm Gaussian reconstruction.
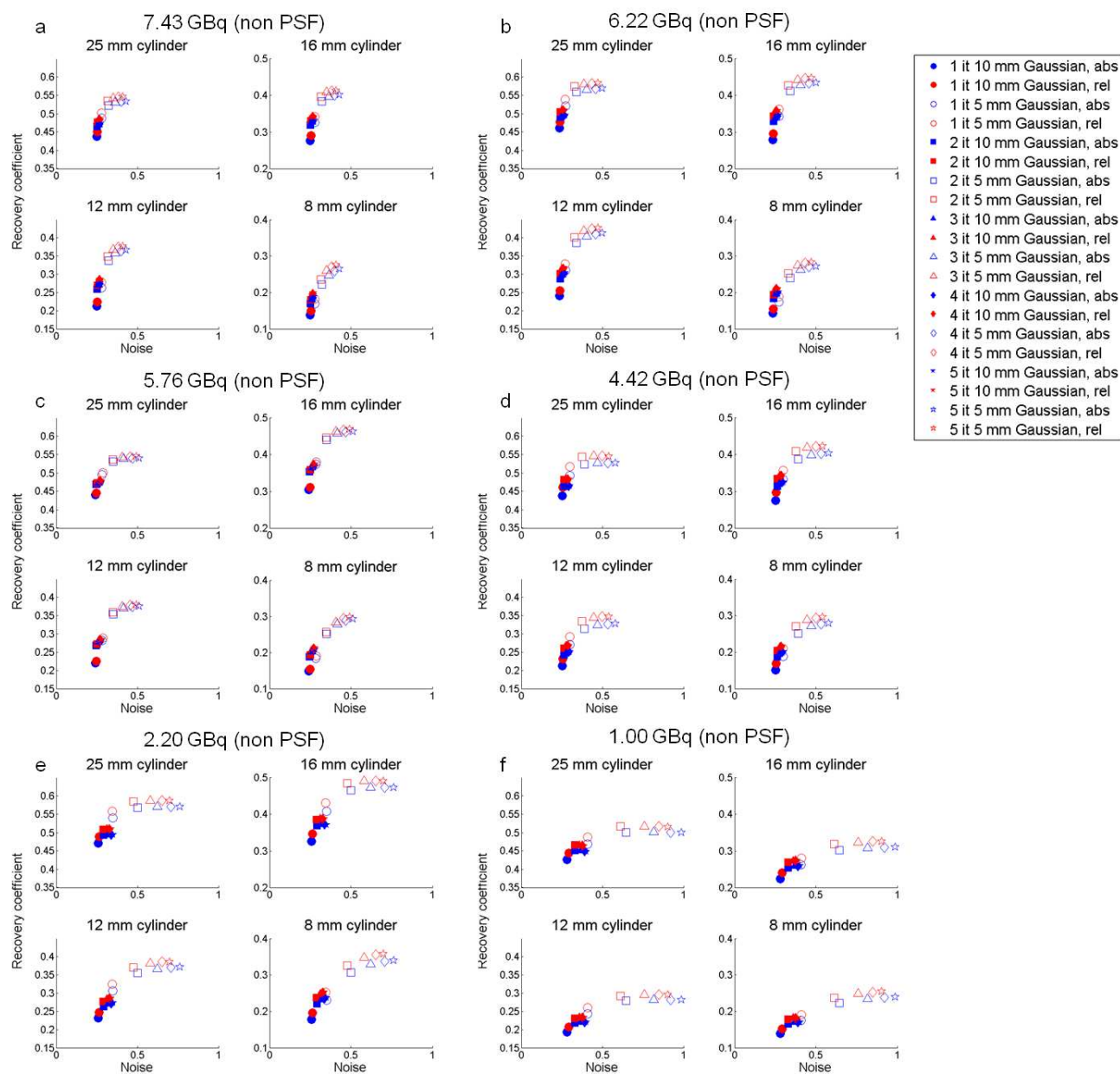
Figure 2.4: Recovery coefficients (RC) versus coefficient of variation of warm background (COV) for each of the four hot cylinders at a range of total activities (1.00-7.43 GBq). Each point represents the RC versus COV measurement for a single non-PSF reconstruction.

Minor improvement in RCs is seen beyond 2 iterations. However, as the number of iterations increases, the noise increases dramatically, especially for the 5 mm Gaussian reconstructions.

23

Optimal activity recovery is thus observed with low number of iterations with moderate noise level. Without PSF compensation, recovery coefficients do not increase markedly beyond 2 iterations on average across all activities and cylinder sizes with a 5 mm Gaussian post-reconstruction filter.

2.3.4   Optimal Reconstruction Parameters with PSF

Figure 2.5 presents the comparison between the optimal reconstruction parameters for non-PSF reconstructions to reconstructions with PSF. Relative change in recovery coefficients and COV of the warm background region were calculated using Eq. 2.4 and 2.3, respectively.
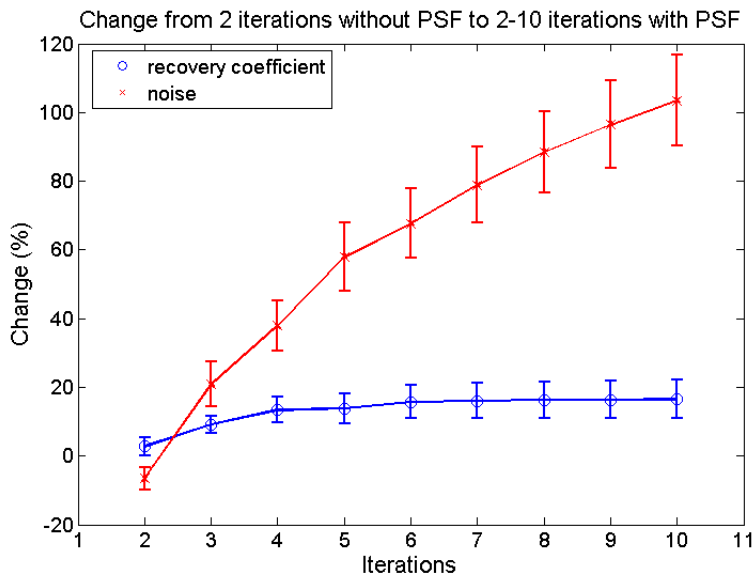
Figure 2.5: Average percent change in recovery coefficients (RC) (blue) and coefficient of variation of warm background (noise) (red) across all hot cylinders and scans from reconstructions with 2 iterations, 5 mm Gaussian without PSF to reconstructions with 2-10 iterations, 5 mm Gaussian with PSF. Error bars represent the standard deviation of percent change across all hot cylinder sizes at both institutions.

On average across all scans and cylinder sizes, there was an increase in the RC with the use of PSF with increasing iteration number. COV was, on average, reduced with the use of PSF for the reconstructions with two iterations. Higher iterations with PSF resulted in higher noise compared to the reconstructions with two iterations without PSF. However, beyond 3 iterations, noise increased at least an additional 20% while the gain in recovery was only an additional 5% more than what it was with 3 iterations. 3 iterations, 21 subsets, 5 mm Gaussian post-reconstruction filter with PSF compensation provided satisfactory images in regards to recovery and noise; although, the recovery was suboptimal (RC<1).
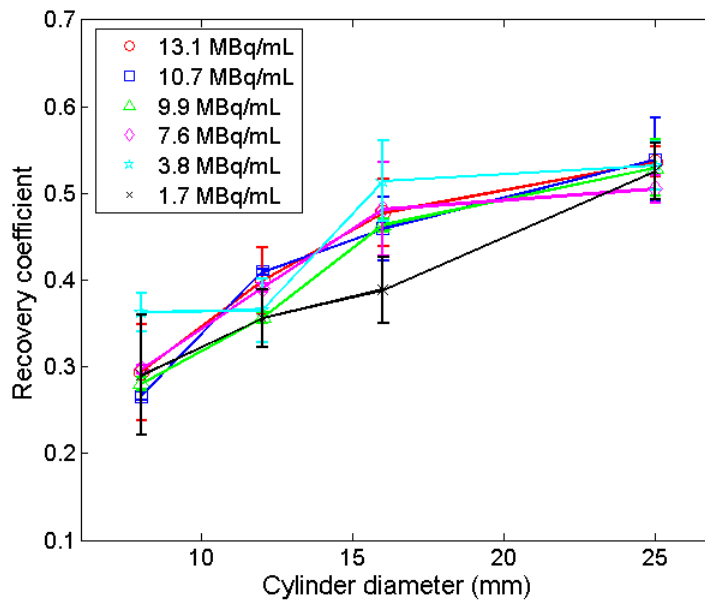
Figure 2.6: Recovery coefficient versus diameter of hot cylinder for several activity concentrations at each institution. Recovery coefficients were measured from PET images reconstructed with the optimal parameter: 3 iterations, 21 subsets, 5 mm Gaussian post-reconstruction filter, and PSF compensation. Error bars represent the range of recovery coefficients measured between institutions.

The difference between the measured total recorded activity in the phantom and true total activity was between -2.05% and -9.26% for this choice of reconstruction parameters. Recovery coefficients measured using this choice of reconstruction parameters for various activity concentrations and cylinder sizes are shown in Figure 2.6.

2.3.5 Effect of Scan Time Duration

The percent change in RCs and noise from 15 minutes to 30 minutes of listmode data are shown in Figure 2.7. The difference in RCs between scan time durations (averaged across the four hot cylinders) tended to be within 10% of each other. Noise however, decreased significantly as scan time increased, especially for the lowest activity scan where noise decreased by as much as 29%.
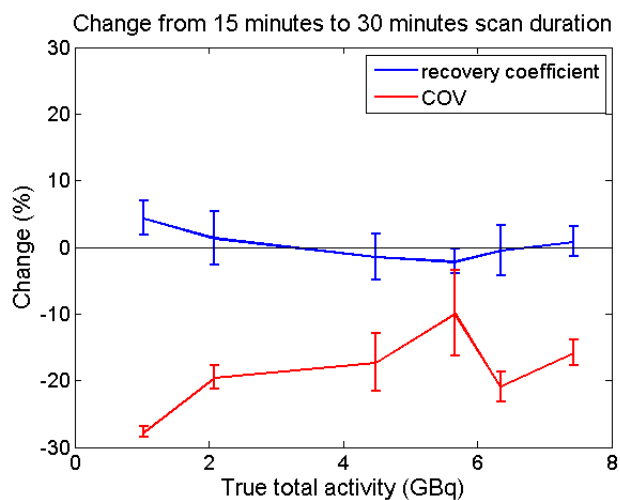
Figure 2.7: Change in RCs and noise from 15 minutes of scan time to 30 minutes of scan time data, averaged across the four hot cylinders at both institutions. (3 iterations reconstruction, 21 subsets, 5 mm Gaussian post-reconstruction filter, with PSF). Error bars represent the standard deviation of percent change across all hot cylinder sizes at both institutions.

26

2.4　Discussion

The simultaneous detection of a Bremsstrahlung photon and an annihilation photon within the same detector may cause a non-linearity in the Trues event detection as a function of activity. In addition, the high Bremsstrahlung photon flux may create an afterglow (or subsiding scintillation after exposure to high radiation field), which may result in spurious counts after removal of the source of activity. The excellent linearity of Singles and Trues with activity as well as the measured versus expected activity in the entire phantom is an indication of absence of detector saturation over the entire range of activity measured, which includes an extreme case of injected activity at nearly 8 GBq.

The differences in absolute count rates between PET/CT (Siemens's Biograph 40) as described by Attarwala et al. [48] and PET/MRI as shown in Figure 2.2 can be attributed to variations in the designs of the different scanners, in particular the detector block size, number of blocks, arrangement of the blocks around the scanner tunnel, the longer axial FOV for the mMR, as well as the coincidence time window. Compared to the Biograph 40, the mMR has more crystals and has a smaller diameter and longer axial coverage, all of which increase the sensitivity of the system. Delso et al. reported a sensitivity of 15.0 kcps/MBq along the center of the mMR [49] and Jakoby et al. reported a sensitivity of 8.1 kcps/MBq along the center of the 4-ring Biograph 40 system [50]. A larger coincidence window (5.86 ns for mMR, 4.5 ns for Biograph 40), together with larger coverage, increases the Randoms count rate on the mMR. The singles rate per block are lower in the mMR, mainly because of the smaller block size (8x8 crystals compared to 13x13 crystals, of the same 4x4x20mm size). All of these differences, especially the relative amount of random events, between PET/CT and PET/MRI along with the low $\beta+$ count rates of ^{90}Y are reasons to investigate the PET components of the two scanners differently and obtain a separate set of PET reconstruction

parameters for ^{90}Y PET/MRI since the noise components are not expected to be same. Due to the high Randoms count rates with respect to the Trues count rates (see Figure 2.2), it is unclear if the convergence properties of the OSEM algorithm will be the same as it is for PET/CT with or without TOF capabilities. At a similar level of counts, theoretically, the reconstruction parameters should be nearly identical for all Siemens Biograph scanners (PET/MRI and PET/CT), since they use the same reconstruction software. Previous studies on a Siemens Biograph mCT PET/CT with TOF and PSF compensation have reported 2 iterations, 24 subsets, and an all-pass filter are optimal when imaging ^{90}Y [37]. With iterative reconstruction methods, convergence tends to speed up with the use of TOF [51], and tends to slow down with PSF compensation [52]. Since the mMR does not have TOF capabilities, a formal phantom study, such as this, was required to find where convergence could be met when imaging ^{90}Y.

The ^{90}Y PET reconstructions with near-maximized recovery coefficients and reduced noise were achieved with 3 iterations, 21 subsets, 5 mm FWHM Gaussian post-reconstruction filter, absolute scatter correction, PSF compensation, and a 30 minute scan time. These results apply for total activity values typically used in patient therapy (17.4 GBq), and a 10:1 activity concentration ratio between hot ROIs and warm background. The difference between measured and true total activity in the phantom using these reconstruction parameters is consistent with the measurements obtained by Willowson et al. on a TOF PET/CT [37]. PSF compensation provided images with higher recovery coefficients than images reconstructed with 2 iterations without PSF compensation. While increasing the iteration number and decreasing the post-reconstruction Gaussian filter size resulted in increased RCs, performing these two operations also significantly increased noise. An increase in noise with the increased number of iterations is characteristic of iterative reconstruction methods [53–55]. In our data, we found that RCs began to reach convergence on average around 2 iterations without the use

28

of PSF compensation and around 3 iterations with the use of PSF compensation. Although the noise increases when going up to 3 iterations with PSF, the benefits of improved accuracy of measurements in terms of RCs is worth the slight cost in increased noise. The highest priority for ^{90}Y PET imaging is to create the most accurate images possible, as defined by the recovery coefficients, which, in turn, will result in the most accurate PET-based dosimetry possible. If maximal activity recovery is achieved, then the second priority is reducing the noise to allow for improved image quality when visualizing the data. Although the noise was slightly lower in the 10 mm Gaussian reconstructions, the benefits in accuracy of measurements from the higher RCs of the 5 mm Gaussian reconstructions was determined to be more valuable. Rigorous ROC analysis with multiple observers is required for an exact choice of optimal reconstructions parameters. We leave this for future work.

Using optimized reconstruction parameters for RC and COV, the 25 mm diameter cylinder's RCs ranged from approximately 0.52–0.60 for activity concentrations of 1.75–13.0 MBq/mL. No apparent positive biases were observed on all measured recovery coefficients, which is likely a consequence of treating the sinograms as separate Prompts and Randoms in the reconstruction. Similar phantom studies have been performed on TOF and non-TOF PET/CT scanners. RCs were reported to be 0.8 for a 37 mm diameter sphere with an activity concentration of 3.9 MBq/mL [32]. Carlier et al. reported RCs to be between 0.6–0.7 for 17–28 mm diameter spheres with an activity concentration of 2 GBq/mL [35]. More recently with the QUEST study, Willowson et al. 2015 reported RCs ranging from approximately 0.1–0.75 from their non-TOF Siemens's Biograph scanners and from 0.2–0.8 with the mCT PET/CT with TOF for spheres ranging from 10–27 mm in diameter. The range of RCs varied depending on the choice of reconstruction parameters. These measurements are consistent with our measurements. The higher reported values on PET/CT could be attributed to larger sphere diameters, higher activity concentrations, and possibly the use of TOF, although further

investigation is required. The higher sensitivity of the PET camera on the mMR, as discussed earlier, may produce results comparable to those from TOF PET/CT if an identical phantom is used between studies. Further investigation is required. Still, RCs were lower than what Willowson et al. reported on the same PET/CT scanner with the high-yielding positron emitter ^{18}F (0.5–1.0 for 10–25 mm diameter sphere) [37]. The reduced recovery coefficient of ^{90}Y relative to ^{18}F may be related to the sparsity of the projection data and high random fractions and point to areas of further investigation on the limitations of 3D-OSEM algorithm for accurate quantitative imaging in those situations [37]. Further investigation is required for optimizing reconstruction algorithms, which may include utilizing the MR for partial volume correction. In any case, such studies could benefit from results presented in our study where base-line reconstruction parameters are first optimized with the standard reconstruction method on the scanner before attempting to improve it further using the MR data.

The absolute scaling scatter correction method is expected to perform better than relative scaling scatter correction when all of the activity is contained within the FOV as long as the activity can be accurately estimated. We observed that absolute scatter scaling performed better than relative scatter scaling for our phantom study and should also perform better than relative scaling with ^{90}Y hepatic radioembolization patients since all of the activity is contained within the FOV. Moreover, given the extremely low counts in the sinogram tails, the fitting and scaling procedure for relative scatter scaling may be more prone to errors and instability. Carlier et al. found similar unreliable results for correcting ^{90}Y PET images when using scatter correction on a Siemens Biograph TruePoint non-TOF PET/CT where relative scatter scaling is the default method [36]. Further investigation is required for the best scatter correction method when imaging patients where parts of the body that still contribute to scatter may extend outside the FOV, such as the arms. Current methods,

such as maximum likelihood reconstruction of attenuation and activity (MLAA), rely on true counts in the sinogram bins where the activity and attenuation are estimated [56]. In the case of ^{90}Y PET imaging, there is no activity uptake in the arms, which means that we cannot estimate attenuation in those bins. One limitation of this study is that we were not able to test the accuracy of MLAA because all of the activity was confined to the FOV. Currently in patient studies, however, we work around the potential inaccuracies of MLAA with ^{90}Y post-radioembolization PET by imaging patients with arms up.

The duration of ^{90}Y PET scans is an important consideration in regards to the practical aspects of the clinical application. Typically, the patients who undergo ^{90}Y radioembolization are ill and have a low tolerance for long-duration scans. Thus, it is desirable to limit the duration of the post-radioembolization imaging as much as possible while still obtaining useful and accurate PET images. Previous PET/CT studies were imaged with either a single bed position with a 15 minute acquisition [20] or with two bed positions, 15–20 minutes each, due to the shorter axial coverage on PET/CT compared to the mMR [37]. The longer axial FOV on the mMR encompasses the entire liver, which allows for a single bed position for our application. As shown earlier in Figure 2.7, the RCs tend to be rather comparable between reconstructions using 15 minutes of listmode data versus those using 30 minutes of data, with slightly higher values for the longer duration scans. However, the noise was much lower in the reconstructions using a full 30 minutes of data, especially for the low 1.00 GBq scan. While many patients receive doses that are at least 1 GBq in activity, many receive doses as low as 0.3 GBq. Scans acquired with these low activities could prove to have unacceptable noise levels if only 15 minutes of listmode data is acquired. Thus, unless a patient received a high amount of activity during treatment, we recommend at least a 30 minute-listmode acquisition on the mMR.

There are several limitations to consider in this analysis. First, there were frequent issues with registration between the MR attenuation maps and the CT attenuation maps, which led to slight registration errors between the PET images and the regions of interest, mostly with the 8 mm cylinder. The 8 mm cylinder often provided the largest discrepancies in measurements not only due to registration errors, but also possibly due to the fact that it is less than twice the FWHM of the PSF of the scanner and only twice the size of the PET crystals. Especially with the high activity scans, partial volume effects were evident with the 8 mm cylinder, more so than the other, larger cylinders. This made registration between the CT images with the ROIs and the PET images from the mMR particularly difficult. The 8 mm cylinder was also difficult to register for the low 1.00 GBq scan, where the activity was so low that it was difficult to find in the PET images.

Another limitation for this study is the lack of simulating challenges inherent to patient attenuation correction with MRI. Since this was a phantom study, and plastic cannot be imaged with MRI, attenuation correction was provided by CT. However, in patient studies, attenuation correction with PET/MRI is provided by the segmentation-based attenuation map obtained from a 2-point Dixon sequence [49]. One of the challenges with this method is accurately classifying lung and bone [46], which both have low proton signal in MRI. Misclassification of tissue in the attenuation map could lead to improper attenuation correction and inaccurate count rate measurements, scatter, and random events estimates. Due to the location of the liver in the lower thorax, there is potential concern for accurate attenuation correction and, subsequently, accurate PET quantification of liver lesion uptake and possible lung uptake when imaging ^{90}Y microspheres with PET/MRI. However, Kim et al., Izquierdo-Garcia et al., and Eiber et al. found that differences between PET standardized uptake values (SUV) measured on segmentation-based MR attenuation corrected PET and CT attenuation corrected PET were within 10% [57–59]. Furthermore, Lau et al. investigated the effects of

lung density in the context of cardiac PET/MR imaging, where lung attenuation correction may be more relevant. Across 30 patients, they found that there was no significant difference between standardized uptake values (SUVs) measured on PET/CT and PET/MRI [60]. Further work is still required for improving the accuracy of MR-based attenuation correction in PET/MRI, especially when imaging regions containing lung and/or bone [46].

The discrepancy of measurements between our two institutions points to the accuracy of PET imaging for accurate quantitative reproducibility in test/retest study. Errors can be attributed in differences in filling the phantom, differences in total activity of the phantom for corresponding scans, and exact positioning of the regions of interest on the images in particular. In order to ascertain the quantitative accuracy and reproducibility on imaging with ^{90}Y, a multicenter study with a standardized phantom and protocol is needed for ^{90}Y PET/MRI as was done for ^{18}F-FDG imaging [61] and for ^{90}Y PET/CT imaging [37]. One institution in the multicenter ^{90}Y PET/CT study performed three consecutive scans of an ACR phantom filled with ^{90}Y solution to test reproducibility of measurements when the scanner and phantom are identical. They measured standard deviations of 4–8% for sphere diameters ranging from 22–37 mm. Our measurements, performed on two separate mMR scanners with separate phantoms and across six different total activity levels had standard deviations for each of the four hot cylinders (8–25 mm diameter) ranging from 3.4–5.8%

We also noticed at both sites that as the activity was allowed to decay over 10 days, activity began collecting on the center insert of the phantom and towards the edges of the cylinders. This phenomenon is likely due to the chloride solution reacting with the acrylic inside the phantom. Mixing a solvent with the solution may have helped prevent this reaction.

A final limitation of this study is that these results are specific to the Siemens Biograph mMR scanner. Further investigation is required to determine if these optimal reconstruction parameters carry over to other PET scanners without TOF capabilities and with PSF compensation.

2.5   Conclusion

Using a phantom filled with ^{90}Y chloride solution, we were able to determine the optimal reconstruction parameters when imaging ^{90}Y with PET on a PET/MRI scanner. If no PSF option is available, reconstructing ^{90}Y PET images from PET/MRI with 2 iterations, 21 subsets, and a 5 mm Gaussian post-reconstruction filter provides an optimized compromise between high RCs and moderate noise for all activity levels and ROI sizes. However, if the PSF option is available, using it can improve the accuracy of measurements at the cost of only a slight increase in noise. With the OSEM–PSF reconstructions, ^{90}Y PET/MRI images should be reconstructed with 3 iterations, 21 subsets, and a 5 mm Gaussian post-reconstruction filter. Furthermore, longer scan times result in higher quality images with significantly reduced noise. Even with these reconstruction parameters, however, there was not perfect recovery of counts in regions of interest <25 mm diameter. This is likely due to current limitations with OSEM software in the context of low positron count statistics and a high random fraction. More work is needed for partial volume correction and image reconstruction methods to further improve quantification accuracy.

Chapter 3

Multi-Institutional Phantom Study for Imaging ^{90}Y with PET/MRI for Post-Radioembolization Dosimetry

3.1 Introduction

Multi-center clinical studies with quantitative end points, typically involve imaging a standard phantom to test quantitative accuracy and inter-center variability. Such a study was performed by Fahey et al. for a multi-center study involving fluorine-18 (^{18}F) on PET/CT [61]. Another similar study was performed by Willowson et al. in the multi-center QUEST Phantom Study for measuring inter-center variability of ^{90}Y on PET/CT [37].

The purpose of this study is to measure both the inter- and intra-center variability of quantitatively measuring ^{90}Y on PET/MR in preparation for a multi-center phase I/II clinical trial. This study mirrors the work that was performed by Willowson et al. in the QUEST study, but focuses instead on PET/MRI scanners.

3.2 Materials and Methods

A total of 7 institutions across 4 countries participated in this phantom study. All sites followed a strict protocol for both filling and imaging the phantom. Three NEMA 2007/IEC 2008 Body phantoms (Data Spectrum, NC) were shared between the seven institutions.

3.2.1 Phantom Preparation

Before filling the phantom with activity, the volume of the background compartment was measured by weighing it with and without water. The phantom was then emptied.

3.6 GBq in 1.4 mL of ^{90}Y chloride solution (PerkinElmer, Waltham, MA) was shipped to each institution from the same batch of ^{90}Y for each round of imaging. The supplier's calibrated activity listed on the shipping document was used as the ground truth for the activity within the vial. Each site recorded the amount of activity reported by their department's dose calibrator for comparison against the reported amount on the shipping label.

The entire contents of the vial were completely emptied into 1300 mL of water with 100 mg of either DTPA or EDTA added to prevent binding of ^{90}Y chloride to the walls of the phantom. Activity was drawn from this solution to fill the 6 spheres (diameters 37, 28, 22, 17, 13, and 10 mm). Once all spheres were filled, the remaining solution was emptied into the background compartment of the phantom, and the remaining volume was filled with water. This resulted in an approximately 8:1 sphere-to-background activity concentration ratio. The center lung insert for the phantom came pre-filled with foam material. The total recorded activity in the phantom was the total activity listed on the shipping document minus any residual activity in the vial and syringe.

3.2.2 Image Acquisition and Reconstruction

The phantom was imaged at 5 time points (Day 0, Day 3, Day 5, Day 7, and Day 10) at each institution on Siemens Biograph mMR PET/MRI scanner, representing a range of total activities from 0.3 GBq–3.0 GBq. These values correspond to the full range of activities administered to patients treated with resin microspheres. The phantom was positioned in a foam cradle with an accompanying positioning device to allow for reproducible placement of the phantom between scans and institutions. The phantom was imaged for 30 minutes in listmode in a single station. The longer field-of-view (FOV) offered by the Biograph mMR allows for encompassing the entire liver in a single station in clinical studies, whereas in PET/CT, 2 stations are typically required. At one of the sites, 3 back-to-back PET acquisitions were performed to evaluate intra-center variability. Another site repeated the phantom filling with 54.4 MBq ^{18}F and imaged at a single time point (15 minutes listmode) for comparison.

All raw PET data were sent via a secure data server (ABX-CRO Advanced Pharmaceutical Services, Dresden, Germany) to a central site in St. Louis, MO for reconstruction and analysis by a single investigator (N.M.). All PET reconstructions were performed using e7tools, the offline reconstruction software provided by Siemens, with a vendor-provided attenuation map of the NEMA 2007/IEC 2008 Body phantom for attenuation correction. The attenuation map was manually inspected and registered for each PET data set. Images were reconstructed with 3D ordinary Poisson ordered subset maximization (OP-OSEM), with the following parameters determined from a previous phantom study: 3 iterations, 21 subsets, 5 mm full-width-half-maximum Gaussian post-reconstruction filter, and absolute scatter scaling correction [44].

3.2.3 Image Post-Processing and Analysis

All image post-processing, including drawing volumes of interest (VOIs) and extracting statistics from those VOIs, was performed in MIM v6.6.7 (MIM Software, Cleveland, OH). VOIs were drawn on the attenuation map of the phantom (see Figure 3.1). The VOIs with their corresponding purpose for quantitative assessment, according to NEMA NU 2-2007 guidelines, are summarized in Table 3.1. Each PET image was fused to the corresponding attenuation map for transfer of VOIs.
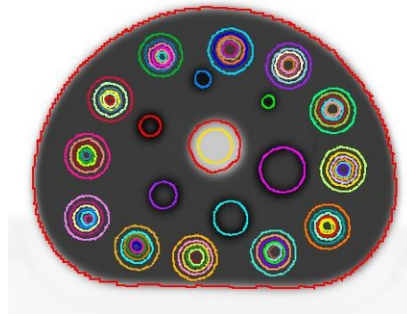
Figure 3.1: Attenuation map of NEMA 2007/IEC 2008 Body phantom with VOIs drawn around each of the 6 fillable spheres, 72 VOIs drawn in the background compartment, and a 28 mm diameter VOI drawn in the cold insert (center, yellow).

Table 3.1: VOI analysis

VOI and size	Measured Quantity	Purpose
Field of View (FOV)	Total activity (Gbq)	Accuracy in total injected activity measurement
Fillable spheres: 37-, 28-, 22-, 17-, 13-, 10-mm	Recovery coefficient of mean activity concentration (MBq/mL)	Accuracy in VOI measurements from partial volume effects
Background spheres: 12 each of 37-, 28-, 22-, 17-, 13-, 10-mm	Recovery coefficient of mean activity concentration (MBq/mL)	Accuracy in warm background VOI measurements
Background spheres: 12 each of 37-, 28-, 22-, 17-, 13-, 10-mm	Standard deviation of mean activity concentration (MBq/mL)	Variability in warm background VOI measurements (noise)
Insert: 28 mm diameter, 160 mm length	Mean activity concentration (MBq/mL)	Misplaced counts

The recovery coefficients (RC) for each of the fillable spheres and respective background VOIs was calculated to assess accuracy of measurements, especially in regards to partial volume effects (PVE):

$$RC(\%) = \frac{A_m}{A_t} \times 100 \tag{3.1}$$

where A_m is the measured mean activity concentration and A_t is the true activity concentration. The coefficient of variation (COV) of RCs for each hot sphere VOI and day of imaging was used to quantify both inter- and intra-center variability:

$$COV_{i,n}(\%) = \frac{\sigma_{i,n}}{\mu_{i,n}} \times 100 \tag{3.2}$$

Background variability for each sphere size s (BV_s) for Day 0 (12 measurements/site $\times$ 7 sites = 84 total VOIs) was calculated using

$$BV_s(\%) = \frac{\sigma_s}{\mu_s} \times 100 \tag{3.3}$$

where σ_s is the standard deviation of the 84 background concentration measurements for a given sphere size s, and μ_s is the average of the 84 background concentration measurements for a given sphere size s.

Activity in the cold insert from background and scatter counts (C_i) were quantified using

$$C_i(\%) = \frac{A_{m,i}}{A_{t,b}} \times 100 \tag{3.4}$$

where $A_{m,i}$ is the measured activity concentration in the cold insert, and $A_{t,b}$ is the true background activity concentration.

3.3 Results

Activities reported by each site's dose calibrator were on average 4.01% lower than that reported on the shipping label (median -5.13%, range -6.31%–0.61%). Figure 3.2 shows PET images from the first day of imaging for each site.
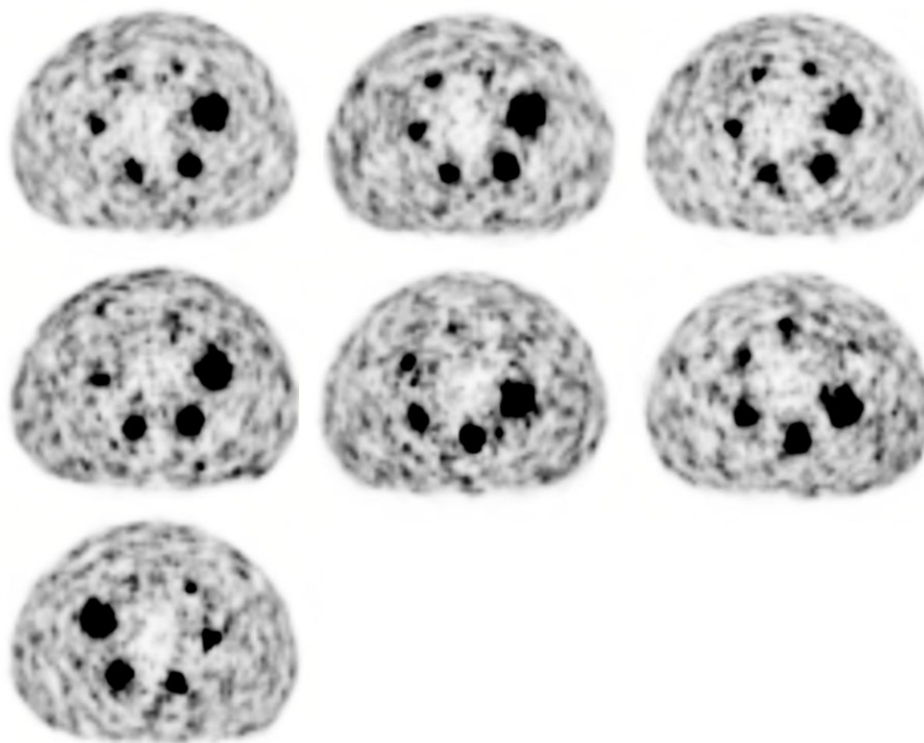
Figure 3.2: PET images from Day 0 for each of the 7 sites.
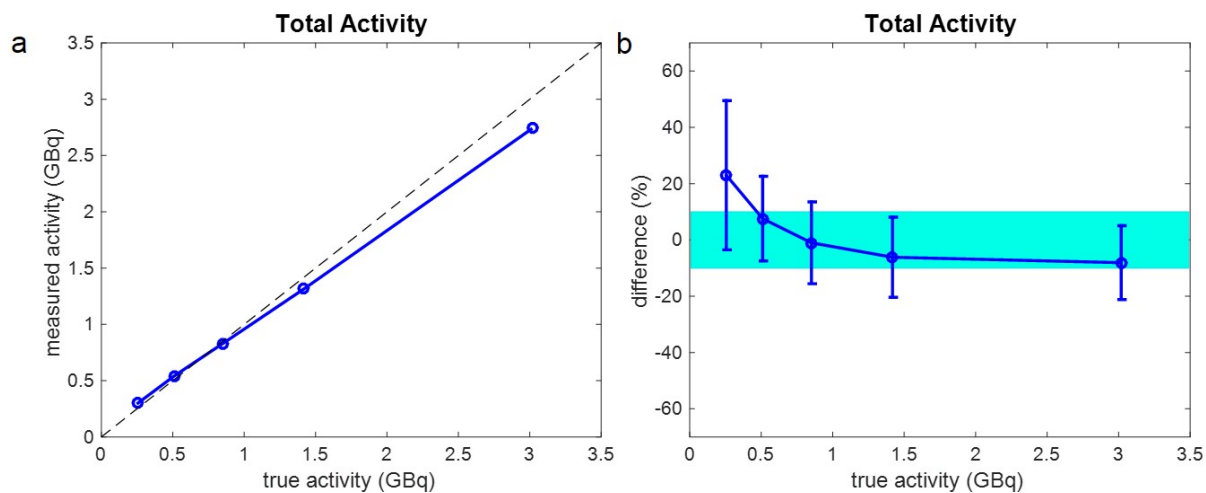
Figure 3.3: (a) Total measured activity within the FOV compared to the true activity. The dashed line represents the identity (i.e. where measured equals true). (b) Error in measured activity within the FOV. Each point represents the mean measured activity. Error bars represent one standard deviation. The shaded region represents +/- 10% error.

Figure 3.3 shows the measured activity versus true activity within the whole FOV. Total activity measured within the FOV had a median error of -2.53% across 35 PET imaging volumes (mean 3.06%, range -23.9%–65%). Most average measurements were within 10% of true activity for activities ≥0.5 GBq. Day 10 overestimated the total activity within the FOV on average by 23.0% (range -20.8%–65.0%).
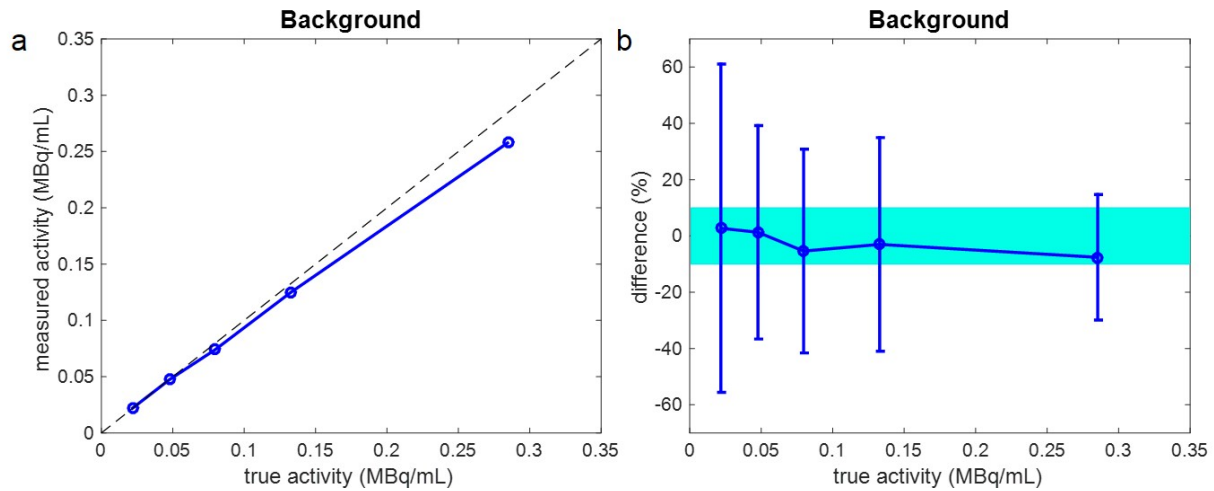
Figure 3.4: (a) Mean activity concentration within the warm background compartment of the phantom compared to the true activity. The dashed line represents the identity (i.e. where measured equals true). (b) Error in measured activity concentration within the warm background. Each point represents the mean measured activity. Error bars represent one standard deviation. The shaded region represents +/- 10% error.

Figure 3.4 shows the mean measured versus true activity concentration in the warm background compartment of the phantom. Mean measured activity concentration had a median error of -9.12% across 2520 warm background VOIs. (mean -2.39%, range -88.9%–311.8%). Day 10 measurements provided the widest range in warm background measurements (range -88.9%–304%).
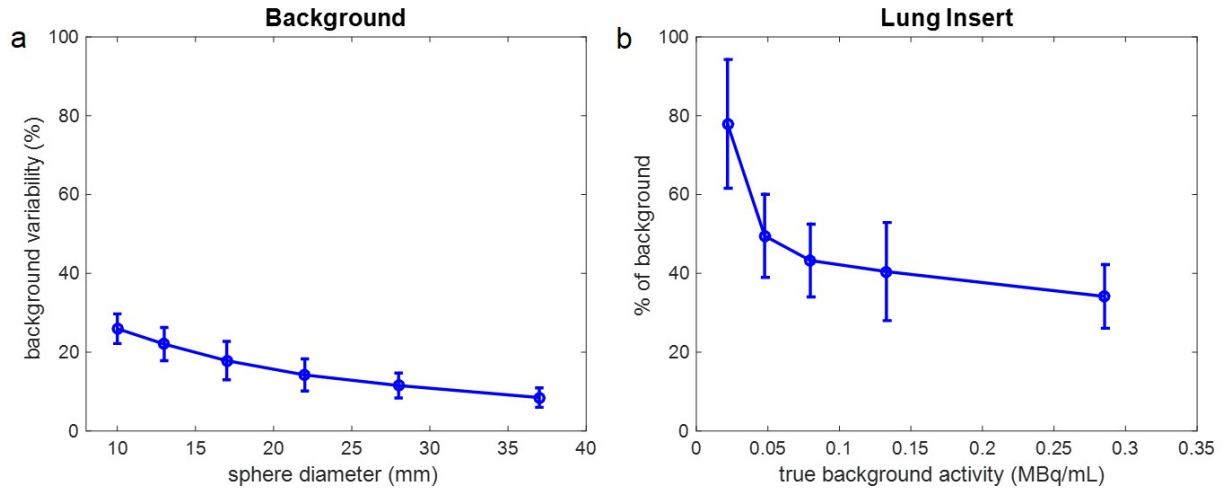
Figure 3.5: (a) Variability in measurements between 12×7 background VOIs for each sphere size. (b) Misplaced counts in cold lung insert reported as percent of true background activity concentration. Each point represents the mean. Error bars represent one standard deviation.

Figure 3.5 illustrates the noise in the PET imaging volumes, quantified by both the background variability (Eq. 3.3) and the scatter/background counts in the cold lung insert (Eq. 3.4). The median background variability across all sphere sizes (total of 504 warm background VOIs) was 16.5% (mean 16.7%, range 6.48%–32.2%), with the least variability for the largest spheres and the highest variability for the smallest spheres. The median C_i for misplaced counts across 35 PET imaging volumes was 42.4% of the true warm background activity concentration (mean 49.0%, range 23.9%–104%).
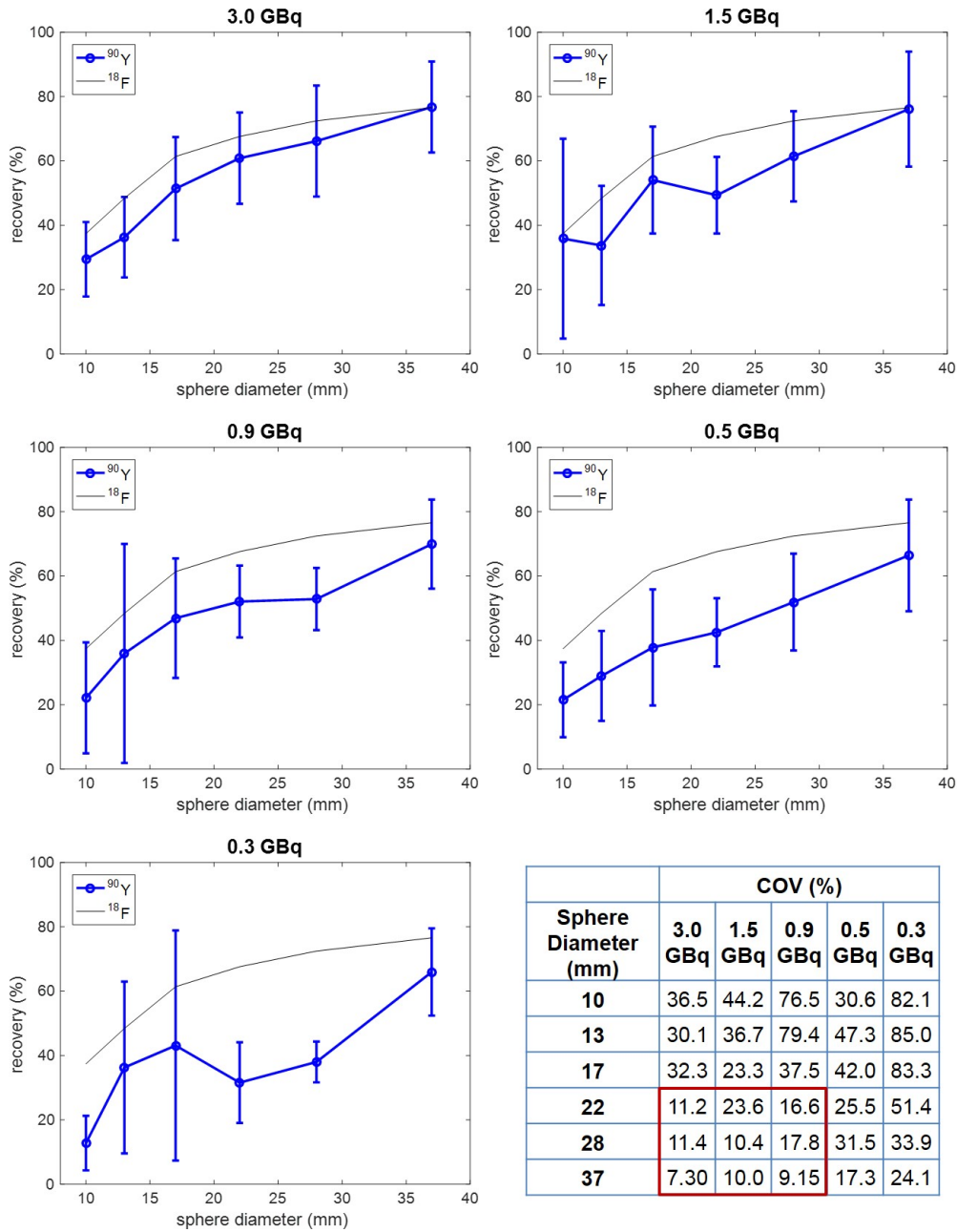
Figure 3.6: Recovery coefficients as a function of hot sphere size from 5 different total phantom activity levels across all sites. Each point represents the mean RC and error bars represent one standard deviation. The COV for each sphere size and total phantom activity level are shown in the included table. COV values <25% are highlighted in the red box. Measurements from one site's ^{18}F measurements (54.4 MBq) are shown in black.

Figure 3.6 illustrates the inter-center variability of imaging ^{90}Y on PET/MRI. The median RC across all 210 hot sphere measurements was 45.7% (mean 46.3%, range 2.63%–118%). The highest mean RC for any given total phantom activity and sphere size was 76.8%, measured from the 37 mm sphere on Day 0. In contrast, the lowest mean RC for any given total phantom activity and sphere size was 12.8%, measured from the 10 mm sphere on Day 10. Agreement with ^{18}F measurements was best on Day 0 and for the largest sphere (37 mm). Variability in measurements increased with decreasing sphere size and decreasing activity.

Sphere Diameter (mm)	COV (%)				
	3.0 GBq	1.5 GBq	0.9 GBq	0.5 GBq	0.3 GBq
10	4.49	40.2	59.4	67.6	108
13	7.58	47.1	39.7	32.9	45.3
17	12.4	9.79	13.4	34.5	49.6
22	5.06	8.35	18.2	36.8	50.8
28	6.48	6.69	4.89	23.9	35.0
37	1.43	4.79	7.52	16.0	20.0
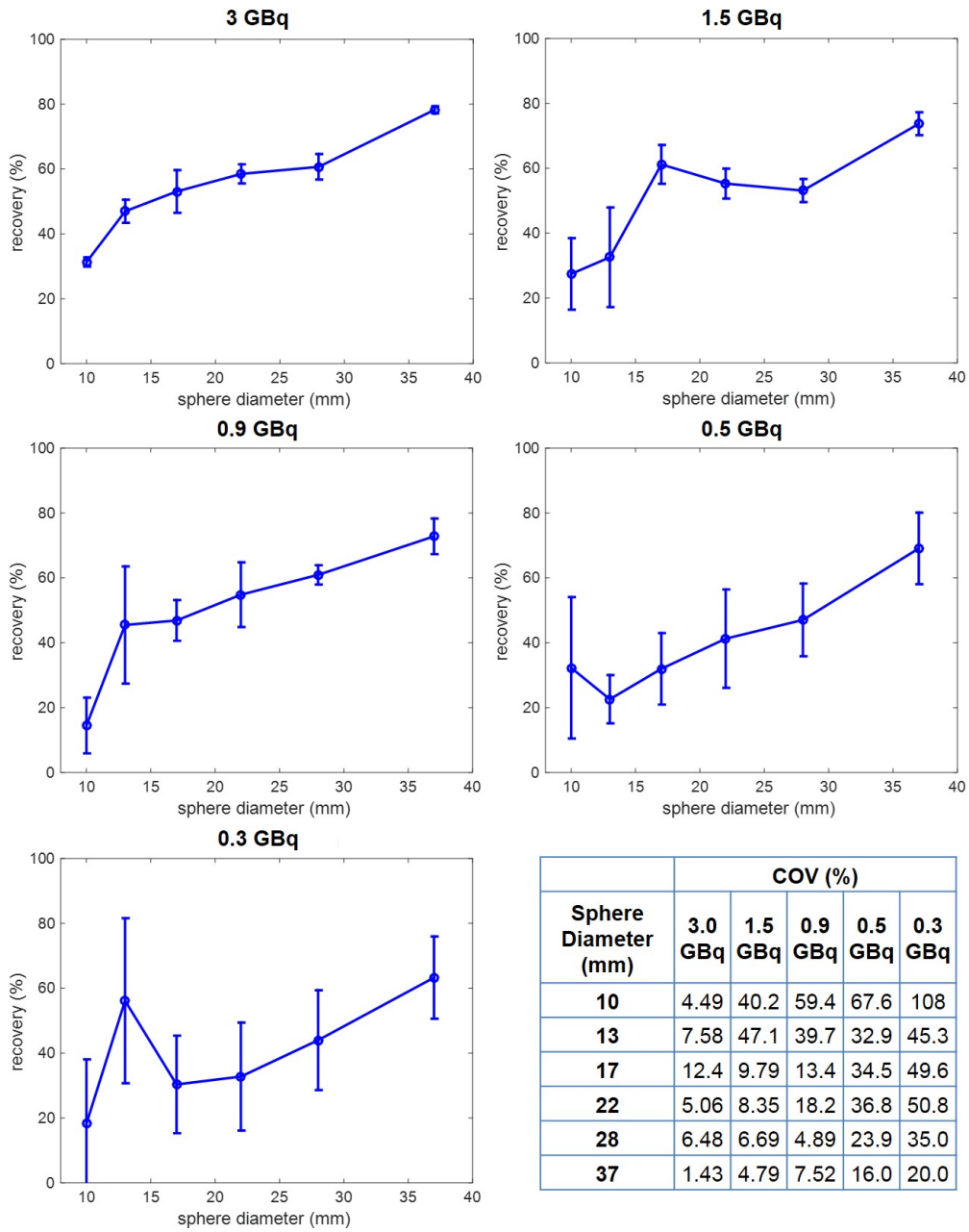
Figure 3.7: Recovery coefficients as a function of hot sphere size from 3 consecutive scans at a single site. Each point represents the mean RC and error bars represent one standard deviation. The COV for each sphere size and total phantom activity level are shown in the included table.

Figure 3.7 illustrates the intra-center variability obtained from one site who acquired three consecutive scans for each imaging day. The median RC across all 90 hot sphere measurements was 50.1% (mean 47.2%, range 4.42%–79.6%). On Day 0, variability between scans for all hot spheres was <13% (mean 6.24%, median 5.77%, range 1.42%–12.4%). All spheres ≥17 mm from scans ≥0.9 GBq in total activity had <20% variability in their RCs. The 37 mm sphere had a variability in measurements ≤20% for all activity levels. Again, variability increased with decreasing sphere size and decreasing activity. Table 3.2 lists the COV for these scans for total activity, background, and cold lung insert. Variability tended to increase with decreasing activity for these VOIs as well.

Table 3.2: Intra-center variability between 3 consecutive scans on each imaging day

	COV(%)				
VOI	**3.0 GBq**	**1.5 GBq**	**0.9 GBq**	**0.5 GBq**	**0.3 GBq**
Total Activity	1.39	0.294	0.275	1.45	1.34
Background	16.8	27.0	27.9	34.6	50.5
Lung Insert	4.67	6.41	2.37	5.44	10.7

3.4 Discussion

Despite the low positron yield from ^{90}Y, PET imaging of this isotope has proven both feasible and useful in previous literature [20,32,34,44,62–64] and is further demonstrated in this work. The results from this study and that reported by Willowson et al. in the PET/CT QUEST study [37] also demonstrate the feasibility of performing multi-institutional clinical studies focused on ^{90}Y PET-based dosimetry.

Even though this multi-institutional phantom study with ^{90}Y PET imaging has been performed previously on PET/CT [37], there are several keys differences between Siemens Biograph PET/CT scanners and Siemens Biograph mMR (PET/MRI) scanners that motivate the need for replicating this study on PET/MRI. First, the Biograph mMR lacks time-of-flight (TOF) capabilities, due to the nature of the avalanche photodiode (APD) detectors, which were utilized for their compatibility with a strong magnetic field. Compared to the Biograph PET/CT scanners, the mMR exhibits increased sensitivity: 15.0 kcps/MBq [49] versus 8.1 kcps/MBq on the Biograph 40 PET/CT [50] due to the geometrical arrangement of the detectors. As discussed previously, the difference in sensitivities is likely due to a longer axial FOV and shorter ring diameter on the Biograph mMR [44]. The tight geometry in mMR results in higher random rates, but the smaller block size results in lower singles rate on mMR [44]. All of these factors, combined with low positron statistics and high Randoms rates (from Bremsstrahlung radiation), make the convergence properties of OSEM unclear between Biograph PET/CT and Biograph PET/MRI scanners. This was demonstrated in our previous phantom study, where we found that the optimal reconstruction parameters, using the same number of subsets, post-reconstruction filter size, and resolution recovery, were at 3 iterations on the mMR instead of 2 iterations for Biograph PET/CT scanners, as suggested by Willowson et al. [37]. Therefore, it is still necessary to demonstrate the quantitative accuracy and test the variability between scanners on mMR, especially since, to our knowledge, this has not been done previously for any isotope on the Biograph mMR.

For Siemens Biograph PET cameras, two modes for listmode acquisitions are available: NETTRUES and PROMPTS+RANDOMS and NETTRUES. NETTRUES involves direct event-by-event subtraction of the delayed coincidences, whereas PROMPTS+RANDOMS involves acquiring separate Prompts and Randoms sinograms, where the Randoms sinogram is obtained via a delayed coincidence window and then smoothed before subtracting from

the Prompts sinogram [37]. In the case of ^{90}Y, which characteristically has high Randoms rates (due to a high flux of Bremsstrahlung radiation) and low Trues statistics (due to a low positron yield), careful handling of the Randoms in the reconstruction proves essential in iterative reconstruction algorithms. In previous generations of OSEM, the non-negativity constraint was often employed [65] and resulted in significant bias in the case of ^{90}Y PET imaging [66, 67]. When using OP-OSEM with PROMPTS+RANDOMS data acquisition [65, 68], there is no subtraction of scatter or Randoms estimates, and therefore, the algorithm always treats positive counts. Thus, there is no need for the non-negativity constraint. However, in situations of very low counts, such with ^{90}Y imaging, the convergence properties of the algorithm may be such that more iterations are needed at the expense of increased noise. In our phantom evaluation [44], we limited the noise in the images by stopping after 3 OSEM iterations (with 21 subsets resulting in 63 updates) and applying a 5 mm Gaussian post-reconstruction filter. Images reconstructed with more iterations and a sharper filter resulted in unacceptably noisy images. This issue has been discussed in the case of ^{90}Y PET imaging, and is likely the cause of lower count recovery compared to standard ^{18}F PET imaging, but has yet to be resolved [36, 37, 44].

Recovery of the total activity within the whole FOV was consistent among sites, with most measurements within +/- 10% of the true values, especially above 0.5 GBq. These values are consistent with those reported by Willowson et al. in the PET/CT QUEST study for 19 Siemens Biograph TOF PET/CT scanners [37], though our reported standard deviation on the Biograph mMR at 0.5 GBq was slightly higher, possibly due to a smaller number of sites. Our total activity results were closer in agreement with the expected activity than those reported for Siemens Biograph non-TOF PET/CT scanners in the same QUEST study, where mean error in the FOV at 0.5 GBq was approximately +20% and standard deviation in this error was approximately +/-60% [37]. Our study was performed an extra scan at a

lower activity level (0.3 GBq) that was not performed in the PET/CT QUEST study. The extra scan at a lower activity level represents the subset of patients who are administered the lowest activity available for resin microsphere treatment. Total activity measurements in this range were, on average, overestimated by >20%, with a standard deviation reaching beyond +/-20%. This trend in overestimation of total activity with decreasing activity has been reported in previous studies using both TOF and non-TOF Siemens Biograph PET/CT scanners [32, 37]. A possible explanation could be extremely low count statistics resulting in higher noise, or artificial peaks in the data, or possibly from non-negativity constraint bias resulting in measured activity higher than the true activity. This effect may be less evident in TOF reconstructions, since it is known that TOF reduces noise not only in better discriminating between True and Random events but also even further by preventing noise propagation in both forward- and back-projections at each iteration [69].

Activity measurements in the warm background compartment of the phantom were excellent, with the mean error consistently <10%. These values are consistent with those reported in the QUEST study for both the Siemens Biograph TOF (>1 iteration, no post-reconstruction filter reconstructions only) and non-TOF PET/CT (PROMPTS+RANDOMS reconstructions only) scanners [37]. However, the standard deviations in our warm background measurements were much higher than those reported in the QUEST PET/CT study. This may be due to our measurements including VOIs of many different spheres sizes (10 mm–37 mm), where the 10 mm VOIs are more susceptible to noise peaks. It was unclear whether the QUEST PET/CT study used only the 37 mm sphere warm background VOIs or all VOI sizes when quantifying the recovered activity in the warm background.

Noise in the PET imaging volumes was quantified by both the background variability on Day 0 (Eq. 3.3) and the scatter/background counts in the cold (no activity) lung insert of

the phantom for each day of imaging (Eq. 3.4). Background variability on the Biograph mMR was significantly lower than that reported for both the TOF and non-TOF Biograph PET/CT scanners in the QUEST study (16.7% mean versus ≈30%, 50%, and 38% means for TOF and Gaussian post-reconstruction filter, TOF and no post-reconstruction filter, and non-TOF reconstructions, respectively) [37]. However, scatter counts in the lung insert from the mMR (49.0% mean) were higher than those from Biograph TOF PET/CT scanners (∼30% mean) and non-TOF PET/CT scanners using PROMPTS+RANDOMS mode (∼35% mean). They were, however, lower than those from Biograph non-TOF PET/CT scanners in NETTRUES mode (∼60% mean) [37]. A possible reason for the higher rate of scatter counts in the cold lung insert compared to those reported by Willowson et al. could likely be the difference in lung inserts. The lung inserts in this study were filled with small polyurethane foam balls whereas those in the QUEST study were made of solid plastic. Furthermore, the attenuation maps from this study were vendor-provided since attenuation maps of phantoms cannot be directly measured with MRI. Depending on the type of lung insert used in the vendor provided maps (filled or solid), this could affect the attenuation properties and scatter estimates used in the reconstruction.

Count recovery in the higher activity concentrated (hot) spheres was good, with mean RCs ranging from approximately 30%–80% on Day 0. These values are consistent with those from a previous ACR phantom study at 2 of the institutions included in this study [44]. They are also consistent with those reported for the same total activity level in the QUEST study for the Siemens Biograph TOF PET/CT scanners (2 iterations, 5 mm Gaussian post-reconstruction filter) and better than those for the non-TOF PET/CT scanners (all reconstructions) [37]. RCs from ^{90}Y PET imaging were also lower than those from ^{18}F PET imaging, with the exception of the largest sphere size on Day 0. We report lower ^{18}F RCs than Willowson et al., who reported RCs approaching near 100% for the largest sphere [37].

Discrepancy in these measurements is likely due to a difference in the method for drawing VOIs: they used a region-growing approach, where VOIs were drawn at 50% of the maximum value, whereas we used the known sphere diameter to draw VOIs. Using an attenuation map-based method for drawing VOIs, as opposed to a region-growing approach, is known to decrease RCs in PET images [32]. Our method is more susceptible to partial volume effects, but is more representative of what is performed for individual lesion dosimetry. As is characteristic of PET imaging studies, whether using ^{90}Y or a standard isotope like ^{18}F, RCs degraded with decreasing VOI size [32, 37, 44, 48]. RCs of any given hot sphere size also slightly decreased with decreasing activity concentration, similar to previous phantom studies [37, 44]. Contributing factors to sub-optimal recovery, especially below ^{18}F, could include partial volume effects, low positron statistics, and high Randoms rates. Low positron statistics, and thus low Trues rates, especially combined with high Randoms rates, are limiting factors of OSEM reconstruction algorithms, as previously discussed. Handling these combined factors in iterative reconstruction algorithms is an active area of research, not just in ^{90}Y PET imaging [36], but also in gated-cardiac PET imaging where statistics are often low [45].

Inter-center variability, as quantified by the COV for each sphere size and total activity level, was acceptable (<25%) for sphere diameters ≥22 mm and total activity levels ≥0.9 GBq. For Day 0, inter-center variability was <12% for sphere diameters ≥22 mm. In the multi-institutional phantom study by Fahey et al., 9 sites tested the variability of imaging ^{18}F on PET/CT using an ACR phantom in preparation for a multi-institutional clinical trial. They reported COVs in RCs of 5.9-, 21.2-, and 17.0% for VOI diameters 25-, 16-, and 12-mm, respectively [61]. Though these values are slightly lower than what we measured for our comparable 22 mm sphere VOI, considering the noisy nature of ^{90}Y PET images, our

results offer promise for the ability to reliably perform multi-institutional clinical studies of ^{90}Y PET-based dosimetry with the Siemens Biograph mMR.

Intra-center variability was also acceptable, $<7\%$ for sphere diameters ≥ 22 mm, which was lower than that reported by the QUEST study for the Biograph TOF PET/CT (5-, 4- and 8% for sphere diameters 37-, 28-, and 22 mm, respectively) on Day 0 [37]. This further emphasizes the reliability of imaging ^{90}Y, even at a single-institution level, since measurements are rather reproducible for VOI sizes ≥ 37 mm or at activities >0.5 GBq.

Several limitations exist with this study. As mentioned previously, we used a vendor-provided attenuation map since direct attenuation map acquisition of phantoms is not possible on PET/MRI scanners. Attenuation maps had to be manually registered to the PET volumes in order to incorporate into offline reconstruction. Manual registration of the attenuation map may have introduced error during the reconstruction procedure. We attempted to mitigate this effect with a phantom cradle and positioning device to replicate phantom placement in the scanner between sites. Furthermore, since we were unable to image the phantom directly with MRI, we could not see if the spheres were filled completely; thus, the "true" activities may have actually been overestimates of what was actually filled in the spheres. Since our RCs agreed well with those reported in the QUEST study by Willowson et al. for Siemens Biograph TOF PET/CT scanners, we consider this effect to be negligible.

PET/MRI scanners from other vendors, such as GE, were not included in this study due to a lack of other vendor sites at the time of conducting this study. Future work will test the performance of GE PET/MRI scanners.

3.5 Conclusion

[90]Y PET measurements from Siemens Biograph mMR (PET/MRI) scanners are acceptable and reproducible at the multi-institutional level. This study may provide insight into the minimum activity level ($\geq$0.9 GBq) and VOI size ($\geq$22 mm diameter) for accurate and reproducible measurements across institutions. Performance is comparable to that of its TOF PET/CT counterpart, and may suggest that multi-institutional clinical studies of ^{90}Y PET-based dosimetry using Siemens hybrid PET scanners can include both PET/MRI and TOF PET/CT scanners, although MRI may offer additional advantages, such as superior soft-tissue contrast for easy delineation of liver lesions.

Chapter 4

PET/MRI of hepatic ^{90}Y radioembolization microsphere deposition predicts treatment response in individual tumors †

4.1 Introduction

The purpose of our study was to assess the feasibility of PET/MRI to evaluate the ^{90}Y microsphere deposition and the resultant dose delivered in individual lesions. The second purpose was to assess whether the measured dose was related to local tumor response. To our knowledge, this is the first series of ^{90}Y PET/MRI patients published with clinical follow-up.

---

†This chapter has been previously published in [70]. htpps://doi.org/10.1007/s00270-015-1285-y © The Author(s) 2015

4.2 Materials and Methods

4.2.1 Patient Sample

Between October 1, 2012 and April 17, 2014, patients undergoing radioembolization for any indication were recruited and consented on an IRB-approved protocol (NCT01744054) for PET/MR imaging on a Siemens Biograph mMR (Siemens Healthcare, Erlangen, Germany). 26 of these patients had imaging follow-up as defined as contrast-enhanced imaging at 3 months or later. Two patients were excluded from analysis due to inability to confidently draw contours around their initial lesion or lesion on follow-up imaging, leaving 24 patients for this analysis. Patient demographics, treatment details and tumor characteristics are listed in Table 4.1. All patients underwent ^{90}Y microsphere delivery pre-treatment evaluation and delivery according to standard procedures. Two patients received whole liver treatment as opposed to standard lobar treatment to prevent further delay of chemotherapy.

Current methods for prescribing radioembolization dose, as recommended by the manufacturer (see Equations 1.1–1.2), differ in part by the particle type (resin versus glass). The average activity delivered to patients was 1.65 GBq (range: 0.4–4.96 GBq), which correlates to a dose of 120–130 Gy in the treated lobe of the liver. An inherent limitation of the current strategies for estimating dose is the assumption of uniform delivery within the segment, section, or lobe to which radioactivity is delivered.

Table 4.1: Patient demographics and treatment information

Tumor Type	Age, Gender	# Tumors	Total Tumor Volume (cc)	Delivery Site (microsphere type)	Delivered Activity (GBq)	PET/MRI Contrast Agent
HCC						
	83, F	1	61.78	Left lobe (resin)	0.7	Eovist
	83, F	1	5.0	Right lobe (resin)	1.03	Eovist
	75, F	1	1514.3	Left lobe (glass)	2.99	Eovist
	61, M	1	157.78	Whole liver (glass)	3.94	Eovist
	77, M	1	185.0	Left lobe (glass)	2.21	Eovist
	62, M	1	549.0	Left lobe (glass)	1.09	Eovist
	74, M	3	376.7	Right lobe (glass)	4.96	Multihance
	73, F	1	27.7	Left lobe (glass)	0.82	Multihance
NET						
	52, M	9	623.6	Right lobe (glass)	2.2	Eovist
	40, M	6	21.0	Right lobe (glass)	0.4	Eovist
	75, M	2	494.6	Left lobe (resin)	0.9	Multihance
	48, F	8	27.7	Right lobe (resin)	0.7	Multihance
mCRC						
	52, M	1	257.8	Right lobe (resin)	1.6	Eovist
	59, M	2	2393.3	Right lobe (resin)	1.4	Eovist
	57, M	3	212.1	Right lobe (resin)	0.9	Eovist
	82, F	2	73.0	Right lobe (resin)	1.0	Eovist
	68, M	4	100.2	Whole liver (resin)	3.2	Eovist
	60, F	10	223.2	Right lobe (resin)	1.0	Multihance
	53, M	3	40.9	Right lobe (resin)	1.6	Multihance
	48, M	12	1681.2	Right lobe (resin)	1.5	Multihance
	54, M	5	356.7	Right lobe (resin)	2.0	Multihance
Esophageal						
	63, M	3	326.4	Right lobe (resin)	1.6	Multihance
Breast						
	57, F	3	39.1	Right lobe (resin)	1.0	Multihance
Thymic Carcinoid						
	49, M	4	529.1	Left lobe (resin)	0.9	Multihance

4.2.2 Post-treatment ^{90}Y PET/MRI Acquisition Parameters

Post-procedural PET/MRI consisted of routine liver sequences (detailed below) and simultaneous PET data acquisition. The PET component consists of 8 rings of 56 detector blocks, each with a 4x4x20 mm LSO (lutetium oxyorthosilicate) crystals with scintillation light readout using avalanche photodiodes. The coincidence window time resolution is 5.86 ns. The spatial resolution is 4.3 mm (reconstructed resolution closer to 6 mm) at FWHM. Imaging was done within 66 hours (range 0.75–66 hours) of ^{90}Y radioembolization based on patient and scanner convenience.

Patients were positioned with arms raised, and 20–40 min of PET data were acquired in a single station to cover the liver and lower thorax. The MR sequences used were a 2-point DIXON for attenuation correction, T2 Turbo spin-echo (TSE) fat-suppressed axial respiratory navigated, in/opposed-phase dual-echo gradient recall T1- weighted, pre–contrast volumetric interpolated breath hold examination (VIBE), dynamic post-contrast VIBE, coronal post-contrast VIBE, diffusion-weighted images (b values 50, 400, 800), axial non-fat-suppressed T2-weighted, radial free-breathing VIBE, and a 20-min delayed VIBE in the axial and coronal planes (for gadoxetic acid enhanced MRI only). Intravenous contrast consisted of gadoxetic acid (Bayer Pharmaceuticals; dose of 0.05 mmol/kg) administered at 1 ml/second or gadobenate dimeglumine (Multihance, Bracco Diagnostics; dose of 0.1 mmol/kg) administered at 2 ml/second.

Tomographic images were generated by iterative reconstruction (3D-Ordered Subset Expectation Maximization (OSEM)) using the following parameters for the Siemens Biograph mMR: 3 iterations, 21 subsets, 172x172 matrix, post-processing Gaussian filter of 5 mm in full width at half maximum, and with point spread function compensation, resulting in a

voxel size of 4.17x4.17x2.02 mm. The parameters for reconstruction were based upon phantom studies conducted at our institution to determine the optimal recovery coefficient with a moderate noise level over a wide range of activity levels [44]. Attenuation correction was derived from the 2-point DIXON MR VIBE sequence (TR = 3.6 ms, TE1 = 2.46 ms and TE2 = 1.23 ms, flip angle of 10deg). Scatter correction was applied using a single scatter simulation technique as provided by the manufacturer. The attenuation of the PET caused by the bed and fixed MRI coils was automatically integrated into the attenuation maps. The scanner was calibrated for absolute activity concentration using a 20 cm diameter ^{68}Ge cylinder containing a known activity concentration and cross-calibrated to the laboratory dose calibrator with a similarly configured ^{18}F-filled cylinder. Since ^{90}Y was not a listed nuclide for PET acquisition on the Siemens Biograph mMR scanner, we used the settings of ^{86}Y for data acquisition and image reconstruction. The scanner calibration factor (ECF) used a ratio of the positron fractions between the selected isotope for scanning (^{86}Y) and ^{68}Ge, and then we manually corrected for ^{90}Y by scaling the reconstructed image intensity by the relative $\beta+$ decay branching ratios and decay constants of ^{86}Y and ^{90}Y. Our previous phantom study with ^{90}Y chloride solution showed that the calibration from ^{68}Ge was accurate [44].

4.2.3   Image Evaluation and Post-Processing

PET and MRI data were reviewed on MimVista (MIM Software, Cleveland, OH) by a board-certified, fellowship-trained MRI radiologist (10 years of experience in abdominal imaging), using rigid registration to align and fuse the liver boundaries. MR sequences were co-registered, and tumor contours, lobar, and whole liver contours were drawn primarily on the Gadoxetic hepatobiliary phase images (20 min delay) or on arterial or portal venous

images for patients who received an alternate contrast agent. Images were assessed qualitatively for expected distribution of dose based on injection site and extrahepatic deposition. Regions of interest were drawn over the paraspinal muscles to derive a background value. Dose maps were calculated by convolution of the activity concentration images from ^{90}Y PET images and a voxelized radiation dose kernel [71]. In short, images were re-sampled on 3-mm cubic voxels, convolved with MIRD-17 3D 3 mm voxel dose-point kernel, and finally re-sampled on the original voxel size, similar to Lea et al. [72]. Image processing was performed using an application written in MATLAB R2012a (Mathworks, Natick, MA). Voxel residence times were calculated using immediate uptake and physical decay only. Based upon the PET-generated dose maps, dose volume histograms (DVH), which plot the minimum dose (Gy) to a given volume (%) of a specified region of interest, were generated for each lesion measuring >1 cm diameter for RECIST criteria and >1 cc for vRECIST criteria. Smaller lesions were not analyzed due to inability to confidently draw contours and identify the lesions on follow-up imaging. To determine treatment response, follow-up imaging was acquired on all patients according to standard-of-care intervals. Contours were drawn around the same lesions as contoured on the initial imaging time point (with initial and follow-up imaging assessed in the same session to allow accurate matching). Standard RECIST criteria were used for differentiating responders ($\geq 30\%$ decrease in the longest tumor diameter), non-responders ($\geq 20\%$ increase in the longest tumor diameter), and stable lesions (else) [73]. A separate analysis using volumetric RECIST (vRECIST) was also used to differentiate responders ($\geq 65\%$ decrease in tumor volume) from non-responders ($<65\%$ decrease in tumor volume or progression).

4.2.4 Statistical Analysis

Summary metrics, including the individual lesion volumes, minimum dose to 20% of the lesion (D20), minimum dose to 70% of the lesion (D70), and average dose (D_{avg}), between responders and non-responders were assessed using a two-sample t test and logistic regression. Results were considered statistically significant at p<0.05. Dose thresholds for assessing response were obtained using receiver operating characteristic (ROC) analysis to determine sensitivity and specificity for response.

4.3 Results

All patients tolerated the imaging procedure without adverse event, and the total time from beginning to end of the PET/MR examination ranged from 42 to 60 min. The fusion of PET and MRI data was accomplished with adequate registration in all cases using rigid registration. The distribution of ^{90}Y microspheres was concordant to injection site in all patients (treated lobe:background SUV_{mean} ratios were significantly greater than 1 for all patients, p<0.001). A single case of extrahepatic deposition was identified due to a patent falciform artery. The patient developed no adverse event related to the deposition. No patients had significant toxicity following ^{90}Y radioembolization treatment.

4.3.1 Response Analysis Based on RECIST

Using standard RECIST criteria, there were 38 responding lesions, 46 stable lesions, and 8 non-responding lesions across the 24 patients. The relationship of DVH and response is shown

in Figure 4.1. D_{avg} and D70 were statistically significant in predicting response between responders and non-responders (p<0.05, see Table 4.2). D_{avg} was statistically significant in predicting response between responders and stable lesions (p<0.05, see Table 4.2); however, D70 was not statistically significant for this response pair (p>0.05, see Table 4.2). No statistical significance was achieved for predicting response between non-responders and stable lesions (p>0.05, see Table 4.2). In an effort to control for any confounding effects, there was no correlation between response and tumor size (p>0.05). Within individual patients, there was heterogeneous response of lesions to treatment (see Figure 4.2a).
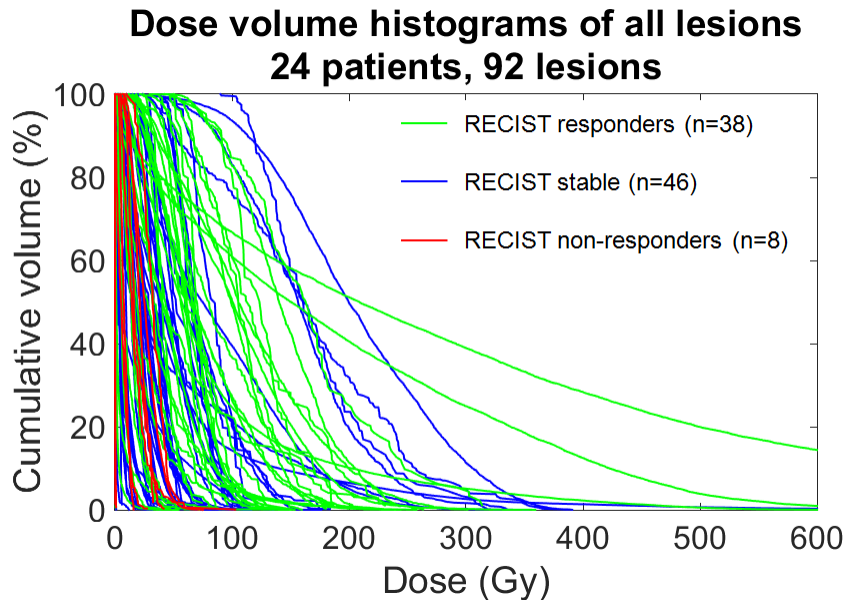
Figure 4.1: Dose volume histograms of all lesions color-coded by response as defined by RE-CIST (Gy=Gray). Davg and D70 are significant for predicting response between responding (green) and non-responding (red) lesions (p = 0.0092 and 0.0063, respectively)

Table 4.2: Factors associated with RECIST response on univariate analysis

RECIST p values from logistic regression analysis	All lesions		mCRC lesions		Hypervascular Lesions	
	D_{avg}	D70	D_{avg}	D70	D_{avg}	D70
Response/progression	0.0092*	0.0063*	0.0452*	>0.05	>0.05	>0.05
Response/stable	0.0291*	>0.05	>0.05	>0.05	>0.05	>0.05
Progression/stable	>0.05	>0.05	>0.05	>0.05	>0.05	>0.05
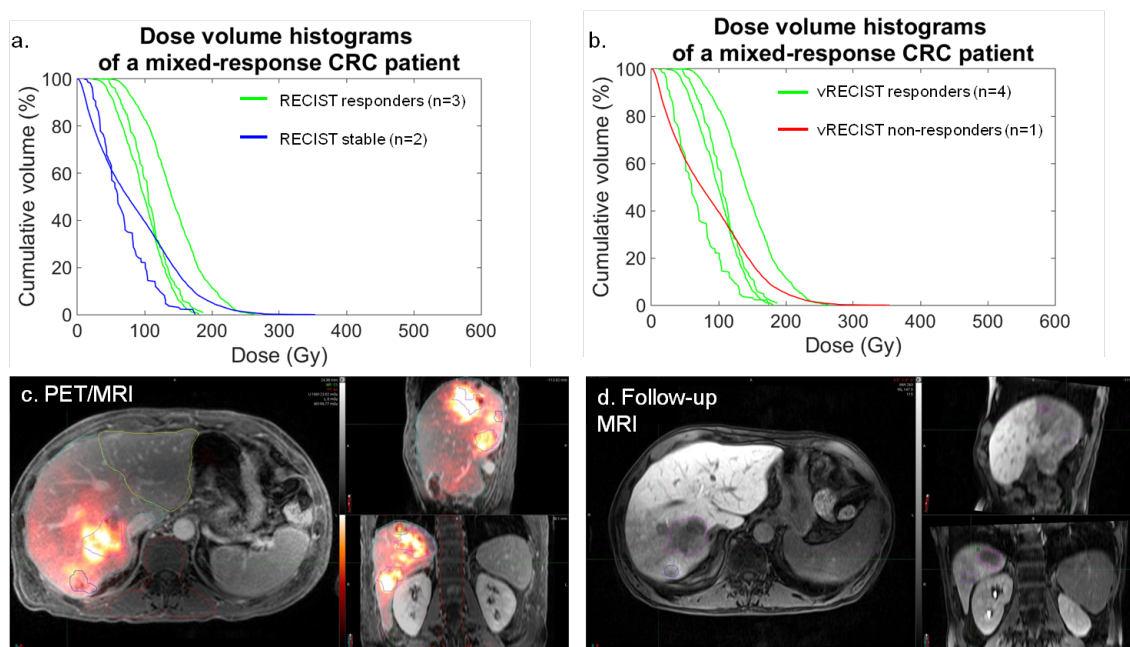
Figure 4.2: Patient with metastatic colorectal carcinoma (mCRC) metastases to the liver showing heterogeneous lesion response following lobar treatment. The DVH shows a mix of responders and stable disease, according to RECIST (A), and responders and non-responders, according to vRECIST (B). The PET/MR fused image (C) demonstrates the contours of different lesions at baseline as well as the overlay of the ^{90}Y microsphere deposition within the treated lobe. Follow-up imaging (D) shows the change in lesion size

Figure 4.3 shows the relationship of DVH and response for mCRC patients (n = 9 patients, 43 lesions). Davg between responders and non-responders was the only quantity that achieved statistical significance for predicting response for the mCRC lesions (p<0.05, see Table 4.2).
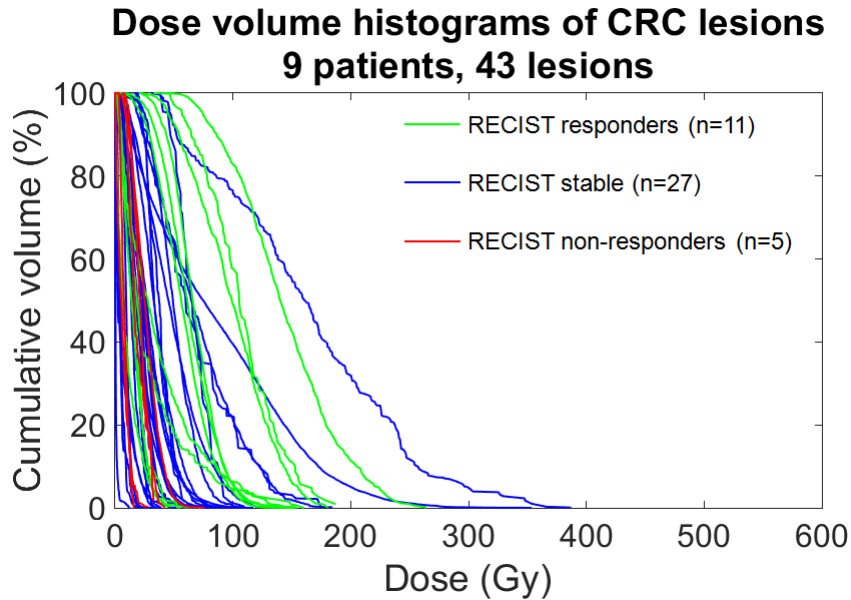
Figure 4.3: Dose volume histograms of colorectal metastases (mCRC) color-coded by response as defined by RECIST. Davg is significant for predicting response between responding (green) and non-responding (red) lesions (p = 0.0452)

Dose volume histograms of hypervascular lesions
13 patients, 42 lesions
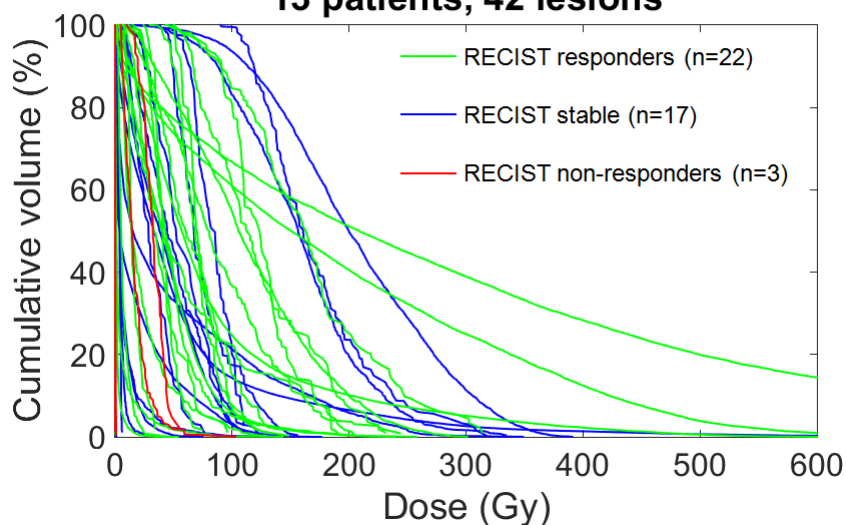
Figure 4.4: Dose volume histograms of hypervascular lesions (HCC, NET, thymic carcinoid) color-coded by response as defined by RECIST. There were no summary statistics that were significant enough to predict response between any of the response categories (p<0.05, see Table 4.2)

Figure 4.4 shows the relationship of DVH and response for hypervascular lesions (HCC, NET, and thymic carcinoid; n = 13 patients; 42 lesions). There was no significant relationship between DVH values and response due to the low number (n = 3) of non-responding lesions. A single HCC lesion represents one of a few outliers in the data and is shown in Figure 4.5 along with the DVH for the lesion. Despite relatively high delivered dose, the lesion did not demonstrate decrease in size and remained primarily enhancing at follow-up imaging acquired 87 days following treatment.
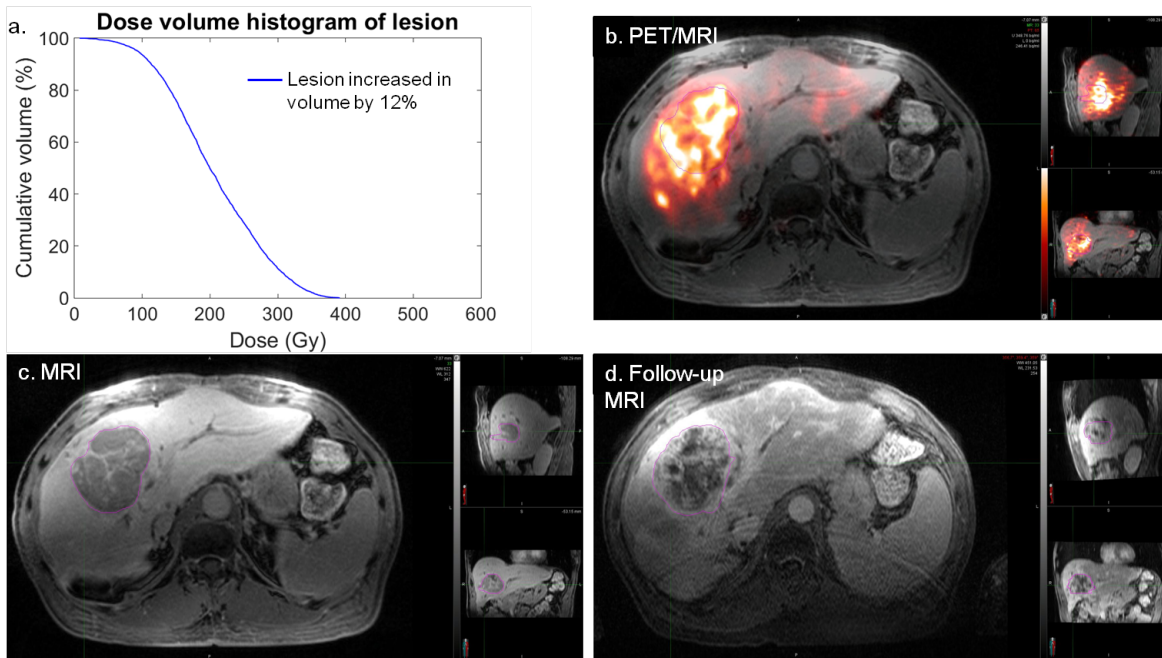
Figure 4.5: Hepatocellular carcinoma (HCC) lesion representing one of the three outliers among the hypervascular lesions (see Figure 4.4). Despite a relatively high delivered dose (A), this lesion did not respond to therapy. PET/ MRI (B) shows expected deposition. Baseline MRI (C) and follow-up MRI (D) show stable/no response as defined by RECIST/vRECIST

4.3.2 Response Analysis Based on vRECIST

Using vRECIST, there were 64 responding lesions and 23 non-responding lesions across the 24 patients. The relationship of DVH and response is shown in Figure 4.6. Both Davg and D70 achieved statistical significance in predicting response (p<0.05, see Table 4.3). Within individual patients, there was heterogeneous response of lesions to treatment (see Figure 4.2b).

Table 4.3: Factors associated with vRECIST response on univariate analysis

| vRECIST p values from logistic regression analysis	All lesions		mCRC lesions		Hypervascular Lesions	
	D_{avg}	D70	D_{avg}	D70	D_{avg}	D70
Response/progression	0.0341*	0.0194*	0.0004*	0.0004*	>0.05	>0.05
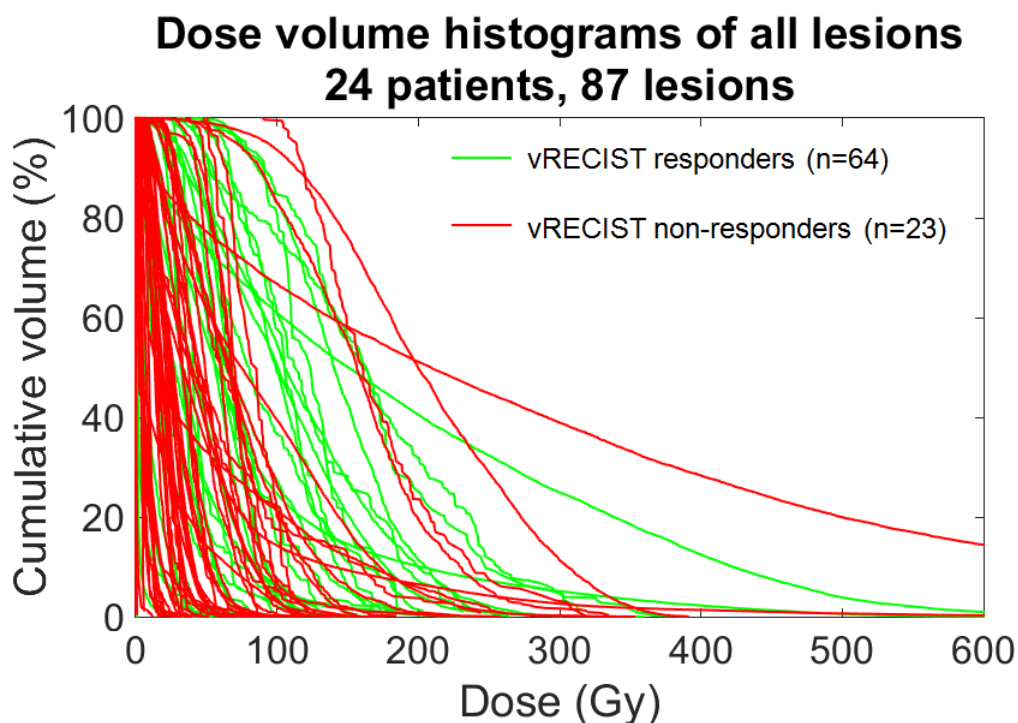
Figure 4.6: Dose volume histograms of all lesions color-coded by response as defined by vRECIST. Davg and D70 are significant for predicting response between responding (green) and non-responding (red) lesions (p = 0.0341 and 0.0194, respectively)

Figure 4.7 shows the relationship between DVH and response for mCRC lesions using vRECIST criteria. Across the 9 patients, there were 25 responding lesions and 17 non-responding lesions. Both Davg and D70 achieved statistical significance for predicting response, with equal p values (p<0.05, see Table 4.3). For mCRC lesions, a Davg of 29.8 Gy provided

76.9% sensitivity and 75.9% specificity for predicting response; D70 of 42.3 Gy provided 61.5% sensitivity and 96.6% specificity for predicting response.
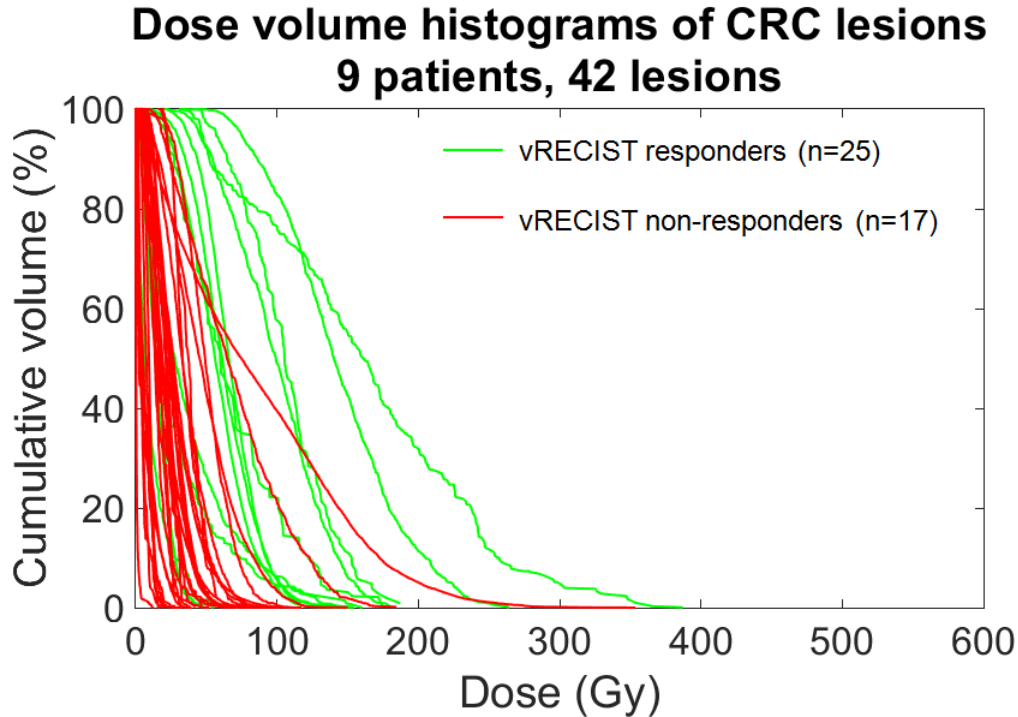
Figure 4.7: Dose volume histograms of metastatic colorectal metastases (mCRC) color-coded by response as defined by vRECIST. Davg and D70 are significant for predicting response between responding (green) and non-responding (red) lesions (p = 0.0004)

Figure 4.8 shows the relationship between DVH and response for hypervascular lesions using vRECIST criteria. Similar to standard RECIST, these lesions did not achieve statistical significance in predicting response (p>0.05, see Table 4.3).
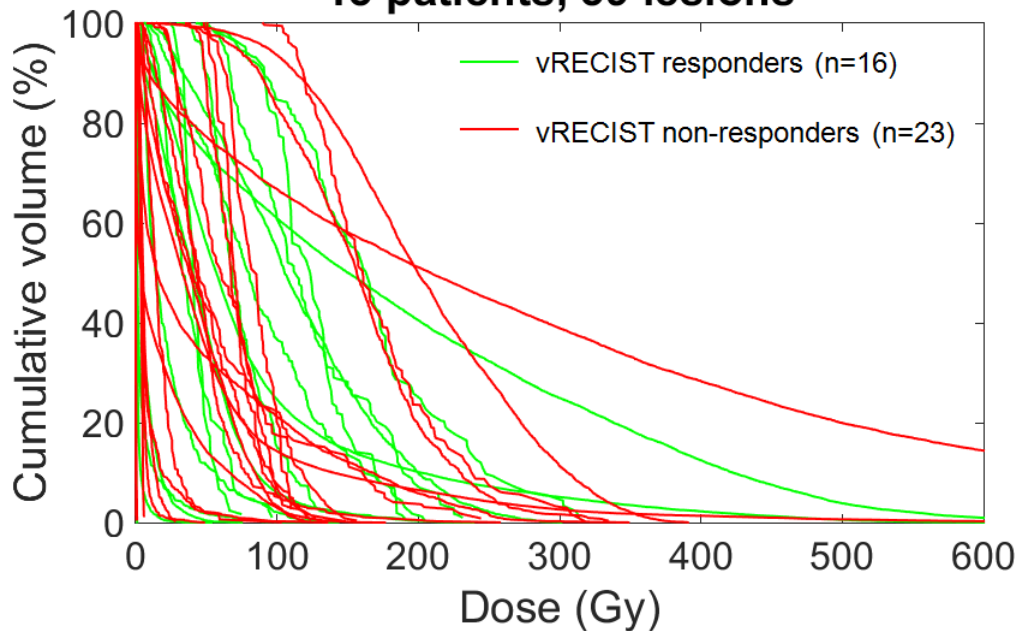
Figure 4.8: Dose volume histograms of hypervascular lesions (HCC, NET, thymic carcinoid) color-coded by response as defined by vRECIST. There were no summary statistics that were significant enough to predict response between any of the response categories (p>0.05, see Table 4.3)

4.4 Discussion

There is growing interest in imaging the delivered activity following ^{90}Y radioembolization both for confirmation of delivery site and quantification of dose [19, 20, 74]. PET imaging appears to be the most reliable and best option, providing higher spatial resolution and more accurate depiction of uptake than ^{90}Y Bremsstrahlung SPECT imaging [19, 62]. In our study, PET/MR imaging of ^{90}Y microsphere distribution demonstrated similar quantitative and qualitative results as previously published with PET/ CT, including the ability to discern extrahepatic deposition [19, 34, 75].

In our study, the DVH was generated to measure dose distribution within tumors. This method has previously been shown to correlate with tumor response [20]; however, the exact metric Davg or D70 remains controversial [22]. When using vRECIST, our results for mCRC patients were significant for Davg and D70 metrics; however, statistical significance was not achieved for D70 when using standard RECIST. Using ROC analysis, we were also able to demonstrate a threshold for vRECIST response in mCRC patients at Davg = 29.8 Gy (sensitivity 76.9%; specificity 75.9%) and D70 = 42.3 Gy (sensitivity 61.5%; specificity 96.6%).

Although RECIST is the standard method for assessing lesion response, Tacher et al. recently found that vRECIST was a more accurate predictor of patient survival following transcatheter arterial chemoembolization (TACE) [76]. In our study, we correlated dosimetric quantities with response using both response criteria. Both RECIST and vRECIST resulted in statistically significant results for predicting response across all lesions and for mCRC lesions. There was a greater significance achieved using vRECIST as opposed to RECIST for mCRC lesions. While vRECIST results were stronger, the average dose was still statistically significant in predicting response between responding and non-responding lesions when using RECIST. Stable disease or disease control, while not the primary goal of therapy, may be a reasonable outcome and was considered as a separate category. Neither vRECIST nor RECIST measurements demonstrated statistical significance in differentiating this category from responders and nonresponders.

The inherent value of DVH analysis is that it captures the heterogeneous nature of ^{90}Y microsphere deposition. Prior studies have shown wide variations in measured tumor and parenchymal ^{90}Y microsphere deposition following lobar administrations [72, 77]. In a recent study, Padia et al. showed heterogeneous ^{90}Y microsphere deposition within tumor and

portal vein tumor thrombus that appeared to correlate with regions of necrosis on follow-up imaging [77]. Srinivas et al. demonstrated wide variability in dose delivered to 98 HCC lesions [78]. The concept of heterogeneous delivery to the parenchyma and tumors may explain heterogeneous response of different lesions within patients who have large tumor burden, as was seen in our study (Figure 4.2-mCRC patient). It is possible that distribution of ^{90}Y microspheres within the target area is highly dependent on locoregional flow factors, injection rate, proximity and complexity of daughter vessel branching, particle load, and cardiovascular dynamics, in addition to inherent tumor vascularity and necrosis. Most current dosing models assume uniform delivery of activity to the treated region/tumor, which is likely a false assumption. Our study confirms the variable dose distribution and is the first to show significant relationship between the DVH in mCRC metastases and response of the lesions on follow-up imaging.

The results of our study represent the first dose-response database generated by PET/MR DVH data for mCRC patients undergoing radioembolization treatment. Future adaptive trials may implicate the findings of post-treatment PET/MRI to achieve adequate tumor coverage. Chang et al. published preliminary data suggesting that quantitative PET/CT following ^{90}Y radioembolization treatment in HCC could achieve more optimized dose coverage (increase in 40 Gy absorbed dose to tumor) and ultimately a complete response [79].

Our study failed to show a similar significant DVH:response relationship in hypervascular lesions (HCC and NET primarily). In the series published by Srinivas et al., the authors likewise failed to show significant correlation between the mean tumor dose and response in 48 evaluable lesions (21 responders, 27 non-responders) [78]. While their results did not reach significance, there was a trend toward greater response and higher dose. Other

authors have demonstrated positive correlation. Kao et al. reported retrospective dose-response information using PET/CT post-treatment DVH analysis, suggesting that complete response could be achieved in HCC patients with a D70>100 Gy and that this dose level was achieved more easily in smaller tumors (<80 cm^3) [20]. The lack of significance in our population may be explained by the outlier HCC case and also the small population size. Further research is needed to confirm the positive results shown by others.

There are several limitations of our study. The dose-response data generated represent that acquired on a lesion-by-lesion basis, which are of great value; however, ultimately patient outcomes and overall survival are better metrics of treatment efficacy. It is our hope that our preliminary results may inform future larger prospective trials with overall survival as the final outcome measure. Another limitation is imperfect registration. While PET/MRI is acquired in a simultaneous manner, improved registration through motion correction algorithms are needed to advance the technological aspects of the study. We were able to achieve satisfactory registration in all cases using MimVista non-deformable registration. Furthermore, in our phantom study and in other phantom studies on PET/CT, recovery for regions 8-37 mm in diameter is only about 50% for ^{90}Y compared to what is recovered when measuring with ^{18}F [37, 49]. Even though point spread function (PSF) compensation was included in the reconstruction process, which has been shown to improve contrast recovery and mitigate partial volume effects in PET images [80], counts were still not completely recovered in the reconstructed ^{90}Y PET images from ours and others phantom studies [44, 78]. Further work with partial volume correction is needed for improving quantitative accuracy, especially for smaller lesions.

Although the results of PET/MR occur after radioembolization, this does not reduce the clinical utility. Immediate predictions (i.e., not waiting for the follow-up imaging study, which

usually does not occur for 3 months following therapy) of tumor response could stratify patient therapy based on lesion prognosis. We would hope that this prediction of response could guide further liver directed or systemic therapies, such as cryoablation, microwave ablation, stereotactic radiation, or changes in chemotherapy. Our results provide preliminary data suggesting that PET/ MRI and volumetric tumor measurements (vRECIST) may provide a useful metric for predicting response in mCRC patients.

4.5 Conclusion

In conclusion, simultaneous PET/MR imaging is a feasible way of determining ^{90}Y microsphere distribution in the liver. Additional work to improve the quantitative nature of this imaging modality is needed. Future clinical and research applications may yield improvements in radioembolization delivery, dosing, and response assessment. This work is now being used as the basis of a clinical trial: Local Ablative Strategies after Endovascular Radioembolization (LASER) (NCT02611661). Patients undergo a PET/MRI scan within 36 hours of radioembolization. Dosimetry analysis is performed where the dosimetric cut-off values determined in this work are used to identify potentially under-dosed lesions. Depending on the number of under-dosed lesions and where they are located in the liver, patients will undergo either radiofrequency/cryo-ablation, stereotactic body radiotherapy (SBRT), or systemic chemotherapy; or, if none are identified to be under-dosed, patients are observed for progression of disease. We continue to accrue patients for this trial.

Chapter 5

Correlation between Pre-Treatment ^{99m}Tc-MAA SPECT and Post-Treatment ^{90}Y PET and Their Role in Predicting Lesion-Specific Response in Hepatic Radioembolization

5.1   Introduction

Pre-treatment planning and imaging is performed with angiography and ^{99m}Tc-MAA SPECT to predict possible extra-hepatic uptake and lung shunting. ^{99m}Tc-MAA SPECT/CT has

proven invaluable for identifying shunts that may lead to extrahepatic non-target embolization. A study by Ahmadzadehfar et al. [81] retrospectively looked at 90 pre-treatment imaging plans across 76 patients and used laboratory testing and physical examination as a reference standard to identify extrahepatic shunting. They reported that ^{99m}Tc-MAA SPECT/CT provided 100% sensitivity and 93% specificity for identifying extrahepatic shunting. This would have resulted in change to treatment plans in 29% of patients.

Despite the success of ^{99m}Tc-MAA SPECT/CT imaging for predicting extrahepatic uptake, there remains controversy as to whether it can predict microsphere localization within tumors and liver parenchyma. While some studies have shown a possible correlation between pre-treatment imaging with ^{99m}Tc-MAA SPECT/CT and clinical outcomes [15, 82–84], only a few have investigated the correlation between quantitative measures of dose on the pre-treatment imaging to dose on direct post-treatment imaging of the microsphere activity distribution [20, 85].

Recent studies have shown ^{90}Y activity distribution imaged with PET, either PET/CT or PET/MRI, is possible due to the small positron yield originating from internal pair production of ^{90}Y decay, which allows accurate depiction of dose delivery [19–22, 34, 63, 64, 70, 85, 86] and higher spatial resolution and therefore higher count recovery as compared to SPECT [19]. However, this imaging takes place after the dose is delivered. If ^{99m}Tc-MAA SPECT data could predict similar dosimetric information, it would be a valuable step in treatment planning.

In this work, we aim to investigate the possible correlation between the ^{90}Y radiation dose extrapolated from the pre-treatment ^{99m}Tc-MAA SPECT and dose measured on the post-treatment ^{90}Y PET. In particular, we aim to compare the predictive abilities of each for tumor response.

5.2 Materials and Methods

A total of 12 patients who underwent standard-of-care ^{90}Y hepatic radioembolization with a standard pre-treatment ^{99m}Tc-MAA SPECT/CT and post-procedural PET/MRI and 36 month follow-up imaging (CT or MRI) at our institution were enrolled in this prospective study. The study was approved by the institutional review board, and all subjects signed an informed consent form (NCT01744054). Patients were treated with resin microspheres (SIR-Spheres, Sirtex Medical, Sydney, Australia), with delivered activity determined by the body surface area (BSA) model, as described on the package insert (see Eq. 1.2). 1 patient received segmental radioembolization, while the rest received lobar radioembolization. Another patient received two treatments, first to the left lobe of the liver, then to the right lobe of the liver 41 days later. A board-certified interventional radiologist retrospectively reviewed the angiograms acquired at the time of ^{99m}Tc-MAA SPECT and ^{90}Y administration to assess the accuracy of the catheter placement. Patients who were classified as having different catheter placement were excluded from the analysis.

5.2.1 Image Acquisition

^{99m}Tc-MAA SPECT/CT pre-treatment imaging was performed following hepatic arterial lobar injection on a Siemens Symbia T6 (Siemens Healthineers, Erlangen, Germany). Images were reconstructed using 2D ordered subset maximization (OP-OSEM) with 8 iterations, 4 subsets, and 8.4 mm full-width-half-maximum (FWHM) Gaussian post-reconstruction filter for a 128 x 128 x 78 image volume with 4.80 x 4.80 x 4.80 mm^3 voxel size. A low dose CT acquired in the same imaging study was used for attenuation correction of the SPECT images.

Patients underwent simultaneous PET and MRI within 66 hours of radioembolization on a Siemens Biograph mMR (Siemens Healthineers, Erlangen, Germany) with arms raised and in a single station to encompass the liver and lower thorax. MRI acquisition included pre-contrast volumetric interpolated breath hold examination (VIBE), standard dynamic post-contrast VIBE in the late arterial phase, portal venous phase, and delayed phases along with a hepatobiliary phase at 20-minutes (for gadoxetic acid enhanced MRI only). Additionally, diffusion weighted imaging (b values 50, 400, 800), axial non-fat-suppressed T2-weighted, T2-weighted fat-suppressed respiratory navigated, T1-weighted in/opposed-phase dual-echo, and a 2-point DIXON sequence for attenuation correction of the PET images (TR = 3.6 ms, TE1 = 2.46 ms and TE2 = 1.23 ms, flip angle of 10deg). PET acquisition was 20-40 minutes of list mode data, reconstructed using ordinary Poisson 3D ordinary Poisson-OSEM (OP-OSEM) with 3 iterations, 21 subsets, 5 mm FWHM Gaussian post-reconstruction filter, absolute scatter scaling correction, and resolution recovery for a 172 x 172 x 127 image volume with 4.17 x 4.17 x 2.02 mm^3 voxel size. Image reconstruction parameters were optimized in a phantom study [44].

5.2.2   Image Post-Processing

Image post-processing was performed using MIM 6 v6.7 (MIM Software, Cleveland, OH). Individual volumes of interest (VOI) were drawn on the contrast-enhanced MR images from PET/MRI around each lesion and around the entire treated lobe of the liver (NM and KF). Lesions <1cc were excluded from the analysis due to lack of confidence of delineation. CT from ^{99m}Tc-MAA SPECT/CT was manually, rigidly registered and fused to the delayed contrast-enhanced MRI from PET/MRI (see Figure 5.1). Registration was optimized to yield best alignment of the treated lobe of the liver and its lesions to maximize the overlap

for these VOIs between both PET and SPECT image sets. Corresponding VOIs were drawn around each lesion on the 3-6 month follow-up imaging studies, which were either contrast-enhanced CT or MRI. Volumetric RECIST (vRECIST) criteria, which has recently been shown to be an indicator of survival, was used to assess response of individual lesions [76]. Lesions that decreased in volume by at least 65% were considered responders, while those that did not were considered non-responders.
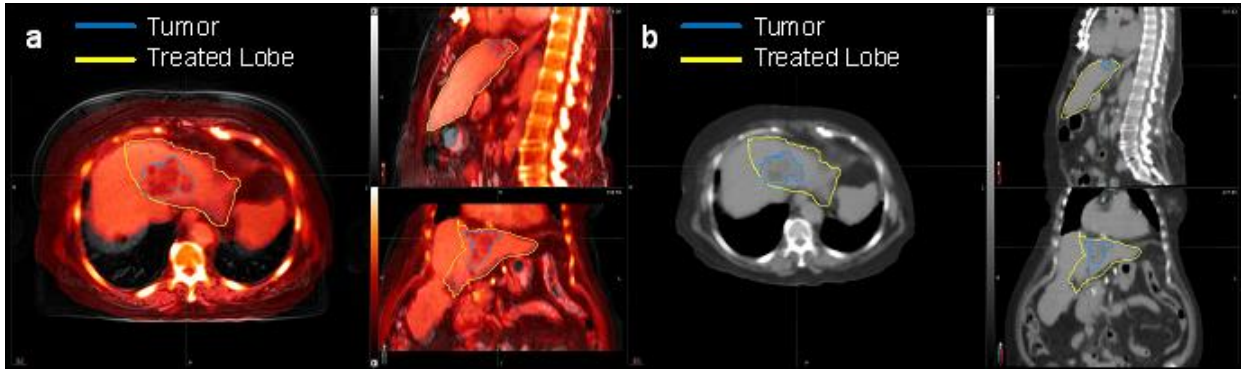
Figure 5.1: Fusion and rigid registration between MRI from ^{90}Y PET/MRI and CT from ^{99m}Tc-MAA SPECT/CT. Registration was aligned toward the treated lobe of the liver and its tumor to allow for adequate registration between these structures.

Three-dimensional (3D) dose maps from ^{90}Y PET and ^{99m}Tc-MAA SPECT were calculated using a dose point kernel (DPK) [71] and local deposition method (LDM) [20,22,82], respectively, using in-house code in MATLAB (MathWorks, Natick, MA). A detailed description of generating 3D dose maps from ^{90}Y PET images is described in our previous study [70]. Due to the inherent lower resolution of ^{99m}Tc-MAA SPECT compared to ^{90}Y PET, we opted to use LDM for calculating extrapolated ^{90}Y dose on the ^{99m}Tc-MAA SPECT images. This method directly scales the voxel values of the SPECT images using an S factor, as opposed to the dose point kernel, which convolves the voxel values with a kernel, thus further blurring the image. We took the S factor to be the sum of all kernel voxels for ^{90}Y with 3 mm

79

cubic voxels, as tabulated in MIRD Pamphlet 17 [71]. ^{90}Y dose extrapolated from ^{99m}Tc-MAA SPECT (D'_{MAA}) was normalized and scaled according to the ^{99m}Tc-MAA counts in the treated lobe of the liver (A_{Tc99m}) and the administered ^{90}Y activity (A_{Y90}, excluding residual) to achieve the extrapolated dose from radioembolization (D_{MAA}) [82]:

$$D_{Tc99m} = D'_{Tc99m} \times A_{Y90}/A_{Tc99m} \qquad (5.1)$$

The dose calculation assumes immediate uptake of the tracer and assumes a residence time determined by the half-life of ^{90}Y (2.67 days) for both methods. Lung shunt fraction determined from the ^{99m}Tc-MAA SPECT scan was not taken into account in the voxel dose calculations since 10/12 patients had a LSF<5% (mean 3.98%, range 1.4% 10.5%). Dose volume histograms (DVH) were extracted from these 3D dose maps within each VOI (lesions and treated lobes). For the remainder of this manuscript, ^{90}Y dose extrapolated from ^{99m}Tc-MAA SPECT images will be referred to as ^{99m}Tc-MAA SPECT dose.

5.2.3   Statistical Analysis

The minimum dose to 70% of the VOI (D70) and average dose (D_{avg}), which have been shown to be predictive of response [20, 70], were compared between ^{99m}Tc-MAA and ^{90}Y doses using Spearman's Correlation test. We also performed Logistic Regression analysis of these metrics to assess the ability of ^{99m}Tc-MAA SPECT and ^{90}Y PET to predict response.

5.3 Results

1 patient with esophageal cancer was classified as having a different catheter placement where the catheter tip was inserted slightly further during ^{90}Y radioembolization compared to the pre-treatment ^{99m}Tc-MAA SPECT. The lesions from this patient were excluded from further analysis. Including the remaining 11 patients, 53 lesions were identified on both PET/MRI and follow-up imaging. These 53 lesions consisted of 37 mCRC (7 patients) and 16 other lesion types (consisting of 2 HCC, 10 neuroendocrine tumor, and 4 thymic carcinoid) (4 patients). A detailed break-down of lesion type and lesion response is in Table 5.1.

Table 5.1: Summary of lesion type and response

	mCRC	Other
Number of lesions	37	16
Responders	*10*	*6*
Non-responders	*27*	*10*
Tumor volume (cc) median	22.65	4.05
(range)	(1.11–947.16)	(1.16–444.02)
^{90}Y administered activity (GBq) median	1.34	0.74
(range)	(0.42–1.03)	(0.9–2.03)

5.3.1 Correlation Between Dose on ^{99m}Tc-MAA SPECT and ^{90}Y PET
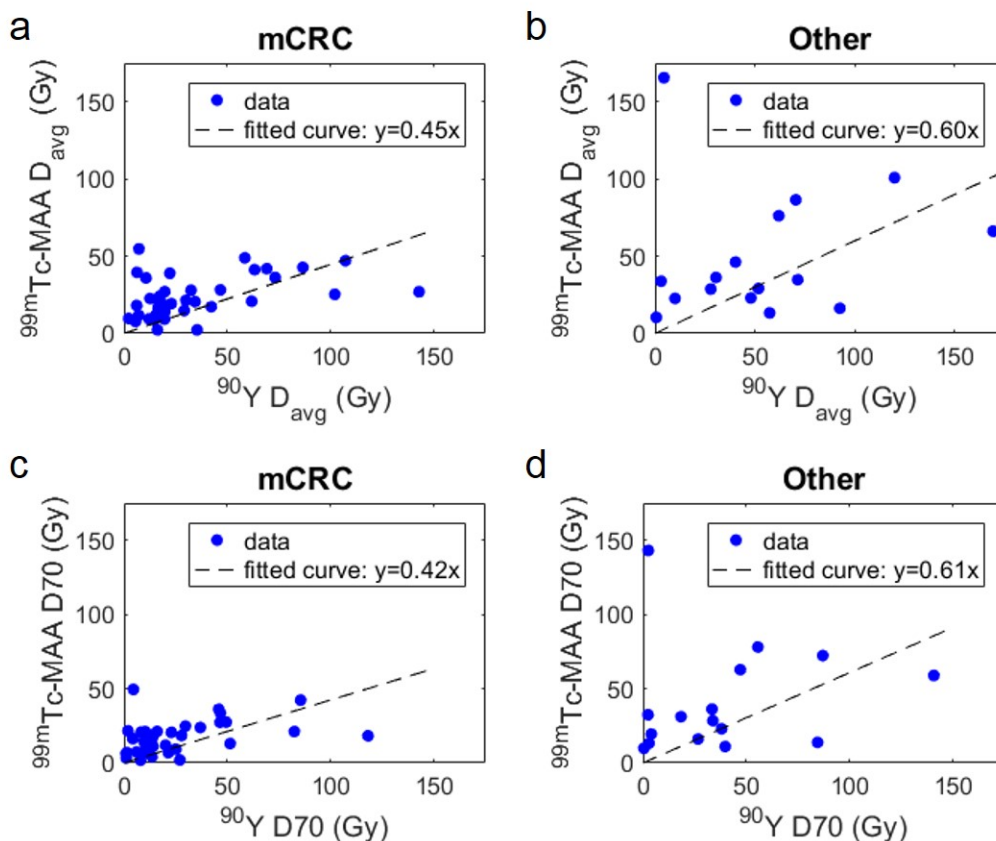
Figure 5.2: Tumor average dose (D_{avg}) and D70 correlation between pre-treatment ^{99m}Tc-MAA SPECT and post-treatment ^{90}Y PET for (a-b) mCRC lesions and (c-d) other lesion types.

Correlations between D_{avg} measured from ^{99m}Tc-MAA SPECT and ^{90}Y PET for individual lesions are shown in Figure 5.2 and summarized in Table 5.2. We observed a weak but statistically significant correlation for Davg and D70 to mCRC lesions between ^{99m}Tc-MAA SPECT and ^{90}Y PET (r = 0.46 and 0.46, p < 0.01). For other lesions, the correlations between ^{99m}Tc-MAA SPECT and ^{90}Y for both average dose and D70 were weaker than

Table 5.2: R- and p-values reporting strength and significance of correlation between dose measured on pre-treatment ^{99m}Tc-MAA SPECT and post-treatment ^{90}Y PET for individual lesions and treated lobe of the liver. *Correlation is significant (p<0.05).

		mCRC		Other		Treated Lobe	
		^{90}Y PET		^{90}Y PET		^{90}Y PET	
		D_{avg}	D70	D_{avg}	D70	D_{avg}	D70
		r-value	r-value	r-value	r-value	r-value	r-value
		(p-val)	(p-val)	(p-val)	(p-val)	(p-val)	(p-val)
^{99m}Tc-MAA SPECT	D_{avg}	0.46* (<0.01)	0.48* (<0.01)	0.30 (>0.10)	0.32 (>0.10)	0.71* (0.01)	0.73* (<0.01)
	D70	0.43* (<0.01)	0.46* (<0.01)	0.28 (>0.10)	0.31 (>0.10)	0.32 (>0.10)	0.53 (0.08)

mCRC and non-significant (r = 0.30 and r = 0.31, p > 0.05), likely due to a single outlier shown in Figure 5.2b and 5.2c and Figure 5.3. This patient showed high ^{99m}Tc-MAA uptake in the outlier lesion (Tumor 1, magenta) on SPECT but not on ^{90}Y PET (^{99m}Tc-MAA D_{avg} = 165.5 Gy, ^{90}Y D_{avg} = 4.46 Gy). This lesion did not respond to treatment. We repeated the statistical analysis, removing this point to test its impact on the results. Removing this point improved the correlation and its significance, but did not make the correlation strong (D_{avg} r = 0.50, p = 0.06 and D70 r = 0.51, p = 0.05).
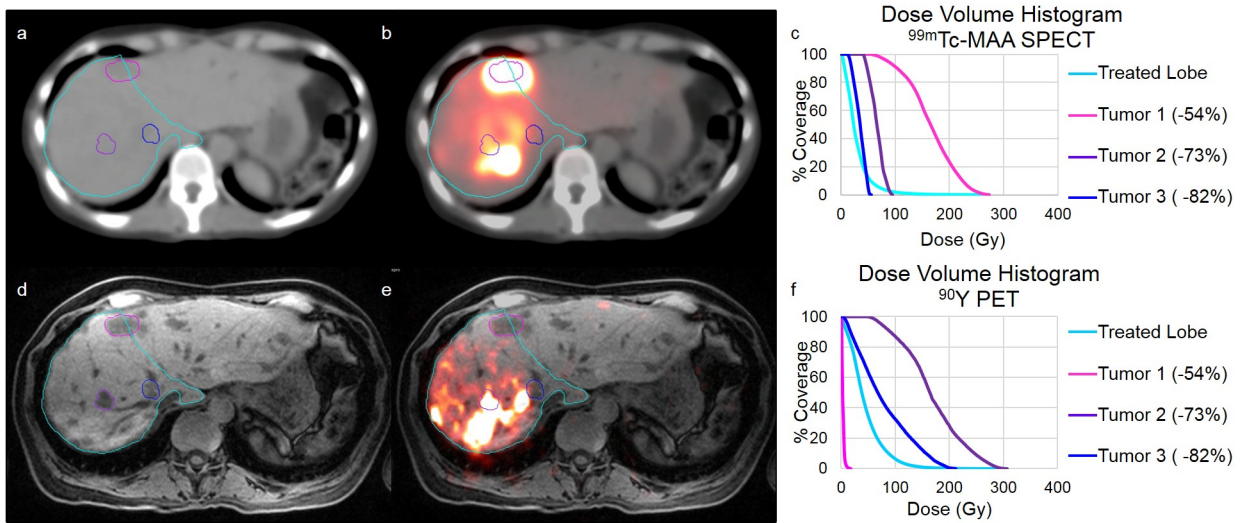
Figure 5.3: 48-yr old female with metastatic pancreatic cancer treated with hepatic radioembolization of ^{90}Y resin microspheres to the right lobe. (a-b) Pre-treatment ^{99m}Tc-MAA SPECT/CT and (c) associated dose volume histogram. (d-e) Post-treatment ^{90}Y PET/MRI and (f) associated dose volume histogram. Percentages in legend indicate the change in lesion volume from radioembolization to follow-up imaging (94 days). Tumor 1 showed a much higher uptake of ^{99m}Tc-MAA than ^{90}Y, whereas Tumors 2 and 3 showed much higher uptakes of ^{90}Y than ^{99m}Tc-MAA.

The correlation for D_{avg} and D70 between pre-treatment ^{99m}Tc-MAA SPECT and post-radioembolization ^{90}Y PET in the treated lobe of the liver is summarized in Table 2 and shown in Figure 5.4. There was a much stronger correlation for D_{avg} in the treated lobe of the liver compared to individual lesions (r = 0.71, p = 0.01). For D70, the correlation in the treated lobe was weaker than D_{avg} and non-significant (r = 0.53, p = 0.08). An example case is shown in Figure 5.3 by the DVH for the treated lobe of the liver. The shape of the DVH was similar between that from ^{99m}Tc-MAA SPECT and ^{90}Y PET, although ^{99m}Tc-MAA dose was consistently lower (^{99m}Tc-MAA D_{avg} = 29.5 Gy and D70 = 16.8 Gy, ^{90}Y D_{avg} = 45.5 Gy and D70 = 25.9 Gy).
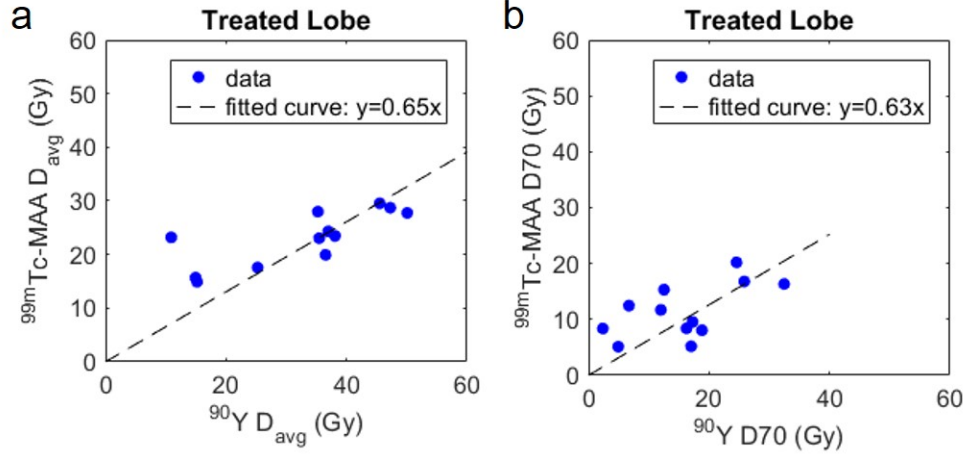
Figure 5.4: Correlation between average dose measured on pre-treatment ^{99m}Tc-MAA SPECT and post-treatment ^{90}Y PET for the treated lobe of liver.

5.3.2 ^{99m}Tc-MAA SPECT and ^{90}Y PET as Predictors for Response

The table of p-values for the ability of initial lesion volume, ^{99m}Tc-MAA SPECT (D_{avg} and D70), and ^{90}Y PET (D_{avg} and D70) to predict individual lesion response is shown in Table 5.3. ^{90}Y PET D_{avg} and D70 were both statistically significant for predicting response for mCRC lesions, while ^{90}Y PET D_{avg} and D70 in other lesions trended for predicting response but did not reach statistical significance. Neither D_{avg} nor D70 from ^{99m}Tc-MAA SPECT were statistically significant for predicting response for any lesion type (p>0.05). Lesion volume was also not significant for predicting response (p>0.05).

Table 5.3: p-values from univariate logistic regression for ^{99m}Tc-MAA and ^{90}Y PET to predict individual lesion response categorized by lesion type (mCRC vs. other). *Values with p<0.05 were considered significant.

		mCRC	Hypervascular
Variable		p-value	p-value
Lesion volume		0.52	0.39
^{99m}Tc-MAA SPECT	D_{avg}	0.92	0.40
	D70	0.69	0.27
^{90}Y PET	D_{avg}	0.02	0.07
	D70	0.02	0.06

5.4   Discussion

Our study reported a small but statistically significant correlation between tumor radiation dose measured on pre-treatment ^{99m}Tc-MAA SPECT and post-treatment ^{90}Y PET for mCRC lesions. The correlation was smaller and non-significant for other lesion types, although this was likely due to a single outlier lesion that did not show ^{90}Y uptake on PET when it was predicted to on ^{99m}Tc-MAA SPECT. This illustrates the importance of performing post-procedural imaging and dosimetry since the ^{90}Y microsphere distribution may be different than was is expected based on pre-treatment ^{99m}Tc-MAA SPECT. However, for the treated lobe of the liver, the correlation for D_{avg} measured on ^{99m}Tc-MAA SPECT compared to ^{90}Y PET was stronger and statistically significant. We also found that ^{99m}Tc-MAA SPECT does not predict individual lesion response for either mCRC or other lesions, while ^{90}Y PET does for mCRC lesions.

More recent literature has proposed the direct measurement of the microspheres after they have been delivered using post-treatment ^{90}Y PET and using this to predict clinical outcomes. Many authors have shown significant predictive ability of ^{90}Y PET as it relates to response and overall survival [21, 63, 64, 70]. While this post-treatment information is important for assessing next steps [86], ideally, a better pre-therapy metric could be used to optimize therapy.

^{99m}Tc-MAA SPECT would be optimally situated as a pre-treatment metric to predict clinical outcomes before the ^{90}Y microspheres are delivered to allow for optimization of treatment. A thorough summary of the literature regarding this topic was recently published by Garin et al. [87] reflects important caveats to this approach. First, much of ^{99m}Tc-MAA SPECT dosimetry is derived from the partition model (MIRD macrodosimetry), which calculates dosimetry based on overall counts within defined compartments (e.g. tumor, target liver, non-target liver) and assumes a uniform distribution [88]. Therefore, unlike voxel-based dosimetry (i.e., as with PET imaging), it does not allow for characterizing the heterogeneity of ^{90}Y microsphere distribution.

In HCC patients, Ho et al. used the partition model to derive tumor and non-tumor compartment doses from ^{99m}Tc-MAA SPECT in 71 patients with unresectable disease treated with resin ^{90}Y microspheres and found that 12/32 patients with a tumor dose >225 Gy achieved partial response (using volumetric WHO criteria), whereas only 4/39 patients with a tumor dose ≤225 Gy achieved partial response [15]. However, some of these patients received multiple treatments depending on residual or recurrent disease, which may have affected the dose-response relationship. Garin et al. also used the partition model on ^{99m}Tc-MAA SPECT for assessing a dose-response relationship in 58 HCC lesions (36 patients) treated with glass ^{90}Y microspheres. They reported that a planned tumor dose of 205 Gy

extrapolated from ^{99m}Tc-MAA SPECT predicted response with 100% sensitivity and 75% specificity [83]. However, upon multivariate analysis, only the corrected dose (correcting for residual ^{90}Y activity at the time of administration) was significant for predicting response. This suggests that accounting for the corrected dose (with residual activity) is essential for using ^{99m}Tc-MAA SPECT to predicting response. Garin et al. also showed a relationship of dose measured on pre-treatment ^{99m}Tc-MAA SPECT with progression-free survival and overall survival in 41 HCC patients with portal vein thrombosis treated with glass microspheres [89]. However, it is important to note that lesions reported in the studies by Garin et al. were large (average diameter > 7.1 cm), possibly making them more likely to take up ^{90}Y activity if they took up ^{99m}Tc-MAA activity. In our study, we only had 2 HCC lesions (61.75 cc and 4.99 cc) across 1 patient (grouped in the other category), limiting our HCC analysis, but these data hint at the complexity of interpreting the effects of pre-treatment SPECT on lesion dosimetry and tumor response, which fueled our interest in using alternative imaging methods.

For metastatic colorectal cancer (mCRC), the results are equally controversial. In patients treated with resin microspheres, Flamen et al. found that absorbed dose of 66 Gy as measured by ^{99m}Tc-MAA SPECT and calculated using LDM predicted metabolic response of the lesions [82]. In another study by Lam et al., ^{99m}Tc-sulfur colloid was used simultaneously with ^{99m}Tc-MAA SPECT for partitioning the liver into functional and non-functional compartments to define tumor VOIs. Dose was calculated using MIRD formalism. They reported that mean tumor absorbed dose >55 Gy resulted in 100% 1-year survival, while <55 Gy resulted in 24% 1-year survival [84]. However, many others have not found such a dose-response relationship for mCRC lesions [90–94].

Similar to previous studies evaluating ^{99m}Tc-MAA SPECT dosimetry for mCRC lesions, we did not find that ^{99m}Tc-MAA could predict response for these lesions, while ^{90}YY PET-based dosimetry could. However, ^{99m}Tc-MAA SPECT may provide some predictive information about general ^{90}Y delivery distribution, as evidenced by the weaker (but significant) correlation for mCRC lesions between ^{99m}Tc-MAA SPECT and ^{90}Y PET.

In our study, neither ^{99m}Tc-MAA SPECT nor ^{90}Y PET could predict response for other lesions, including HCC, NET, and thymic carcinoid, though our study may have been underpowered. These three lesion types were grouped together during statistical analysis due to the small numbers of each type. Our results are similar to those previously reported by Song et al. comparing dosimetry from pre-treatment ^{99m}Tc-MAA SPECT and post-treatment ^{90}Y PET in 22 patients—16 HCC, 3 cholangiocarcinoma, 4 metastatic disease—using the partition model instead of voxel-based dosimetry. They found that although doses to tumor measured from both methods were significantly correlated (r = 0.64, p<0.01), ^{99m}Tc-MAA SPECT was unable to predict progression-free survival while ^{90}Y PET could [85]. An earlier study by Kao et al. found that ^{99m}Tc-MAA SPECT-based dosimetry, using the partition model, was predictive of ^{90}Y PET-voxel-based dosimetry [20]. Their analysis, however, included only 7 HCC lesions, and was very selective, only including lesions that had a tumor to normal ratio >2.

In our study we did find a stronger and statistically significant correlation for treated lobe dose suggesting that ^{99m}Tc-MAA SPECT can be used for predicting total liver dose, allowing clinicians to increase or decrease the planned dose if there are concerns of under-dosing the lesions or of radiation-induced liver toxicity, respectively. Similar results were reported in the study by Song et al. where the correlation was strong and highly significant (0.71, p<0.001). Criteria for well-tolerated maximal dose to the liver was introduced by Garin et al. when the

dosimetry cut-off value of 205 Gy was used to boost the injected activity if the tumor dose was predicted to be <205 Gy as determined from ^{99m}Tc-MAA SPECT [95]. They found that among 71 patients with HCC, a combination of healthy infused liver dose >120 Gy and hepatic reserve <30% were statistically significant associated with grade III or higher liver toxicity [95]. Further work is needed for investigating the correlation between ^{99m}Tc-MAA SPECT and toxicity events in patients with other types of cancer.

Our report indicates that the pre-treatment MAA distribution differs substantially from the treatment of ^{90}Y microsphere distribution despite all efforts made to replicate the exact positioning of the catheter tip in the hepatic arterial system. Possible explanations for mixed results regarding correlation between doses measured from the pre-treatment ^{99m}Tc-MAA SPECT and ^{90}Y PET as well as response may be due to the difference in particle sizes between MAA and ^{90}Y microspheres, injection rates, and changes in flow dynamics. While it is not possible to correct for difference in particle size, we did attempt to correlate catheter location between MAA and ^{90}Y to eliminate this potential source of variability. Beyond these practical issues of delivery, there are also challenges with the technical acquisition of the ^{99m}Tc-MAA SPECT, where different methods of correction for scatter, attenuation, and collimator response can affect the quantitative accuracy of this technique [96].

Our study has some limitations including its small size and retrospective nature. ^{99m}Tc-MAA SPECT analysis was performed on standard SPECT imaging without extra reconstruction correction factors, and registration errors may have introduced bias in VOI propagation between the PET and SPECT images. Furthermore, although not necessarily a limitation, we used voxel-based dosimetry (DPK and LDM), which allows for characterization of the heterogeneous activity distribution, whereas many other groups used an overall absorbed dose method (MIRD or partition model). We also performed lesion-by-lesion analysis as opposed

to overall tumor volume analysis, thus allowing for characterizing individual lesions that may have shown high uptake on ^{99m}Tc-MAA SPECT but not on ^{90}Y PET, as demonstrated in Figure 5.3, or vice-a-versa.

5.5 Conclusion

^{99m}Tc-MAA SPECT-based dosimetry was well correlated with ^{90}Y PET-based dosimetry for the treated lobe of the liver. Whether this can be used to guide decisions for increasing or decreasing the planned amount of ^{90}Y administered activity should be an area of future research. The ^{99m}Tc-MAA SPECT imaging was not a strong predictor of response in either mCRC or other lesion types in our study.

References

[1] Cancer.Net, "Liver cancer: Statistics," 2015.

[2] American Cancer Society, "Cancer facts and figures," 2015.

[3] A. Ananthakrishnan, V. Gogineni, and K. Saeian, "Epidemiology of primary and secondary liver cancers," *Semin Intervent Radiol*, vol. 23, no. 1, pp. 47–63, 2006.

[4] J. Wagner, M. Adson, J. Van Heerden, M. Adson, and D. Ilstrup, "The natural history of hepatic metastases from colorectal cancer. a comparison with respective," *Annals of Surgery*, vol. 199, no. 5, pp. 502–8, 1984.

[5] Emory Liver Center, *Malignant Liver Tumors*. 2013.

[6] S. M. Ibrahim, P. Nikolaidis, F. Miller, R. Lewandowski, R. Ryu, K. Sato, S. Senthilnathan, A. Riaz, L. Kulik, M. Mulcahy, R. Omary, and R. Salem, "Radiologic findings following Y90 radioembolization for primary liver malignancies," *Abdominal Imaging*, vol. 34, pp. 566–581, 2009.

[7] R. Murthy, R. Nunez, J. Szklaruk, W. Erwin, D. Madoff, S. Gupta, K. Ahrar, M. Wallace, A. Cohen, D. Coldwell, A. Kennedy, and M. Hicks, "Yttrium-90 microsphere therapy for hepatic malignancy: Devices, indication, technical considerations, and potential complications," *RadioGraphics*, vol. 25, pp. S41–S55, 2005.

[8] C. Eipel, K. Abshagen, and B. Vollmar, "Regulation of hepatic blood flow: The hepatic arterial buffer response revisited," *World Journal of Gastroenterology*, vol. 16, no. 48, pp. 6046–6057, 2010.

[9] A. Saxena, B. Meteling, J. Kapoor, S. Golani, M. Danta, D. Morris, and L. Bester, "Yttrium-90 radioembolization is a safe and effective treatment for unresectable hepatocellular carcinoma: a single centre experience of 45 consecutive patients," *International Journal of Surger*, vol. 12, no. 12, pp. 1403–8, 2014.

[10] D. Kooby, V. Engatashvili, S. Srinivasan, A. Chamsuddin, K. Delman, J. Kauh, C. Staley, and H. Kim, "Comparison of yttrium-90 radioembolization and transcatheter arterial chemoembolization for the treatment of unresectable hepatocellular carcinoma," *J Vasc Interv Radiol*, vol. 21, no. 2, pp. 224–230, 2010.

[11] G. Nace, J. Steel, N. Amesur, A. Zajko, B. Natasi, J. Joyce, M. Sheetz, and T. Gamblin, "Yttrium-90 radioembolization for colorectal cancer liver metastases: a single institution experience," *International Journal of Surgical Oncology*, vol. 571261, 2011.

[12] P. Gibbs, V. Heinemann, and N. Sharma, "SIRFLOX: Randomized phase III trial comparing first-line mFOLFOX6 $\pm$ bevacizumab (bev) versus mFOLFOX6 + selective internal radiation therapy (SIRT) $\pm$ bev in patients (pts) with metastatic colorectal cancer (mCRC)," *Journal of Clinical Oncology*, vol. 33 (suppl; abstr 3502), 2015.

[13] M. Vouche, R. Salem, F. Miller, M. Lemort, B. Vanderlinden, D. De Becker, A. Hendlisz, and P. Flamen, "Y90 radiomebolization of colorectal cancer liver metastases: response assessment by contrast-enhanced computed tomography with or without PET-CT guidance," *Clin Imaging*, vol. 39, no. 3, pp. 453–62, 2015.

[14] J. Bilbao and M. Reiser, "Liver radioembolization with ^{90}Y microspheres," *Medical Radiobiology: Diagnostic Imaging*, 2008.

[15] S. Ho, W. Lau, T. Leung, M. Chan, P. Johnson, and A. Li, "Clinical evaluation of the partition model for estimate radiation doses from yttrium-90 microspheres in the treatment of hepatic cancer," *European Journal of Nuclear Medicine*, vol. 24, no. 3, pp. 293–8, 1997.

[16] J. Campbell, C. Wong, O. Muzik, B. Marples, M. Joiner, and J. Burmeister, "Early dose response to yttrium-90 microsphere treatment of metastatic liver cancer by a patient-specific method using single photon emission computed tomography and positron emission tomography," *Int J Radiat Oncol Biol Phys*, vol. 74, no. 1, pp. 313–20, 2009.

[17] M. Elschot, J. Nijsen, M. Lam, J. Prince, M. Viergever, M. van den Bosch, B. Zonnenberg, and H. de Jong, "^{99m}Tc-MAA overestimates the absorbed dose to the lungs in radioembolization: a quantitative evaluation in patients treated with microspheres ^{166}Ho-microspheres," *Eur J Nucl Med Mol Imaging*, vol. 41, no. 10, pp. 1965–75, 2014.

[18] S. Ng, V. Lee, M. Law, R. Liu, V. Ma, W. Tso, and T. Leung, "Patient dosimetry for ^{90}Y selective inernal radiation treatment based on ^{90}Y PET imaging," *Journal of Applied Clinical Medical Physics*, vol. 14, no. 5, pp. 212–221, 2013.

[19] Y. Kao, J. Steinberg, Y. Tay, G. Lim, J. Yan, D. Townsend, A. Takano, M. Burgmans, F. Irani, T. Teo, T. Yeow, A. Gogna, R. Lo, K. Tay, B. Tan, P. Chow, S. Satchithanantham, A. Tan, D. Ng, and A. Goh, "Post-radioembolization yttrium-90 PET/CT-part 1: diagnostic reporting," *Eur J Nucl Med Mol Imaging Research*, vol. 3, no. 56, pp. 1–13, 2013.

[20] Y. Kao, J. Steinberg, Y. Tay, G. Lim, J. Yan, D. Townsend, C. Budgeon, J. Boucek, R. Francis, T. Cheo, M. Burgmans, F. Irani, R. Lo, K. Tay, B. Tan, P. Chow,

S. Satchithanantham, A. Tan, D. Ng, and A. Goh, "Post-radioembolization yttrium-90 PET/CT-part 2: dose response and tumor predictive dosimetry for resin microspheres," *Eur J Nucl Med Mol Imaging Research*, vol. 3, no. 57, pp. 1–12, 2013.

[21] M. D'Arienzo, "Emission of $\beta+$ particles via internal pair production in the $0+ - 0+$ transition of ^{90}Zr: Historical background and current applications in nuclear medicine imaging," *Atoms*, vol. 1, no. 1, pp. 2–12, 2013.

[22] A. Pasciak, A. Bourgeois, J. McKinney, T. Chang, D. Osborne, S. Acuss, and Y. Bradley, "Radioembolization and the dynamic role of ^{90}Y PET/CT," *Frontiers in Oncology*, vol. 4, no. 38, 2014.

[23] M. Sarfaraz, A. Kennedy, M. Lodge, X. Li, X. Wu, and C. Yu, "Radiation absorbed dose distribution in a patient treated with yttrium-90 microspheres for hepatocellular carcinoma," *Med Phys*, vol. 31, no. 9, pp. 2449–2453, 2004.

[24] D. Chan, N. Alzahrani, D. Morris, and T. Chua, "Systemic review and meta-analysis of hepatic arterial infusion chemotherapy as bridging therapy for colorectal live metastases," *Surgical Oncology*, vol. 24, no. 3, pp. 162–71, 2012.

[25] A. Kennedy, D. Ball, and S. Cohen, "Hepatic imaging response to radioembolization with yttrium-90-labeled resin microspheres for tumor progression during systemic chemotherapy in patients with colorectal liver metastases," *Journal of Gastrointestinal Oncology*, vol. 6, no. 6, 2015.

[26] R. Stock, N. Stone, and A. Tabert, "A dose response study for I-125 prostate implants," *Int J Radiat Oncol Biol Phys*, vol. 41, pp. 101–108, 1998.

[27] United States, "Enforcement of the U.S. Department of Veterans Affairs brachytherapy program safety standards: Hearing before the subcommittee on oversight and investigations of the committee on veterans affairs, House of Representatives, 111th Cong," 2009.

[28] R. Nath, W. Bice, W. Butler, Z. Chen, A. Meigooni, V. Narayana, M. Rivard, and Y. Yu, "AAPM TG 137: AAPM recommendations of dose prescription and reporting methods for permanent interstitial brachytherapy for prostate cancer," 2009.

[29] B. Eaton, H. Kim, E. Schreibmann, D. Schuster, J. Gait, B. Barron, S. Kim, Y. Liu, J. Landry, and T. Fox, "Quantitative dosimetry for yttrium-90 radionuclide therapy: tumor dose predicts fluorodeoxyglucose positron emission tomography response in hepatic metastatic melanoma," *J Vasc Interv Radiol*, vol. 25, no. 2, pp. 288–95, 2014.

[30] N. Kokabi, J. Galt, M. Xing, J. Camacho, B. Barron, D. Schuster, and H. Kim, "A simple method for estimating dose delivered to hepatocellular carcinoma after yttrium-90 glass-based radioembolization therapy: preliminary results of a proof of concept study," *J Vasc Interv Radiol*, vol. 25, no. 2, pp. 277–287, 2014.

[31] L. Strigari, R. Sciuto, S. Rea, L. Carpanese, G. Pizzi, A. Soriani, G. Iaccarino, M. Benassi, G. Ettorre, and C. Maini, "Efficacy and toxicity related to treatment of hepatocellular carcinoma with 90Y-SIR spheres: radiobiologic considerations," *J Nucl Med*, vol. 51, no. 9, pp. 1377–85, 2010.

[32] K. Willowson, N. Forwood, B. Jakoby, A. Smith, and D. Bailey, "Quantitative 90Y image reconstruction in PET," *Med Phys*, vol. 39, no. 11, pp. 7153–7159, 2012.

[33] J. Oppenheimer, "On the internal pairs from oxygen," *Physics Review Letters*, vol. 60, p. 164A, 1941.

[34] V. Gates, A. Esmail, K. Marshall, S. Spies, and R. Salem, "Internal pair production of ^{90}Y permits hepatic localization of microspheres using routine PET: Proof of concept," *J Nucl Med*, vol. 52, no. 1, pp. 72–76, 2011.

[35] T. Carlier, R. Eugène, C. Bodet-Millin, E. Garin, C. Ansquer, C. Rousseau, L. Ferrer, J. Barbet, F. Schoenahl, and F. Kraeber-Bodéré, "Assessment of acquisition protocols for routine imaging of Y-90 using PET/CT," *Eur J Nucl Med Mol Imaging Res*, vol. 3, no. 1, p. 11, 2013.

[36] T. Carlier, K. Willowson, E. Fourkal, D. Bailey, M. Doss, and M. Conti, "90Y-PET imaging: Exploring limitations and accuracy under conditions of low counts and high random fraction," *Med Phys*, vol. 42, no. 7, pp. 4295–4309, 2015.

[37] K. Willowson, M. Tapner, D. Bailey, and QUEST Investigator Team, "A multicentre comparison of quantitative ^{90}Y PET/CT for dosimetric purposes after radioembolization with resin microspheres," *Eur J Nucl Med Mol Imaging*, vol. 42, no. 8, pp. 1202–22, 2015.

[38] B. Pichler, A. Kolb, T. Nägele, and H. Schlemmer, "PET/MRI: Paving the way for the next genereation of clinical multimodality imaging applications," *J Nucl Med*, vol. 51, no. 3, pp. 333–336, 2010.

[39] T. Frankel, R. Do, and W. Jamagin, "Preoperative imaging for hepatic resection of colorectal cancer metastasis," *Journal of Gastrointestinal Oncology*, vol. 3, no. 1, pp. 11–18, 2012.

[40] H. Seo, M. Kim, J. Lee, W. Chung, and Y. Kim, "Gadoxetate disodium-enhanced magnetic resonance imaging versus contrast-enhanced 18F-f luorodeoxyglucose positron emission tomography/computed tomography for the detection of colorectal liver metastases," *Invest Radiol*, vol. 46, pp. 548–55, 2011.

[41] A. Muhi, T. Ichikawa, U. Motosugi, H. Sou, H. Nakajima, K. Sano, M. Sano, S. Kato, T. Kitamura, Z. Fatima, K. Fukushima, H. Iino, Y. Mori, H. Fujii, and T. Araki, "Diagnosis of colorectal hepatic metastases: comparison of contrast-enhanced CT,

contrast-enhanced US, superparamagnetic iron oxide-enhanced MRI, and gadoxetic acid-enhanced MRI," *J Magn Reson Imaging*, vol. 34, no. 2, pp. 326–35, 2011.

[42] D. Sahani and S. Kalva, "Imaging the liver," *The Oncologist*, vol. 9, no. 4, pp. 385–397, 2004.

[43] K. Beiderwellen, L. Geraldo, V. Ruhlmann, P. Heusch, B. Gomez, F. Nensa, L. Umutlu, and T. Lauenstein, "Accuracy of [18F]FDG PET/MRI for the detection of liver metastases," *PLoS ONE*, vol. 10, no. 9, p. e0137285, 2015.

[44] N. Maughan, M. E. M. Conti, K. Knesaurek, D. Faul, P. Parikh, Z. Fayad, and R. Laforest, "Phantom study to determine optimal PET reconstruction parameters for PET/MR imaging of 90Y microspheres following radioembolization," *Biomed Phys Eng Express*, vol. 2, p. 015009, 2016.

[45] A. Martinez-Möller, M. Souvatzoglou, G. Delso, R. Bundschuh, C. Chefd'hotel, S. Ziegler, N. Navab, M. Schwaiger, and S. Nekolla, "Tissue classification as a potential approach for attenuation correction in whole-body PET/MRI: evaluation with PET/CT data," *J Nucl Med*, vol. 50, no. 4, pp. 520–6, 2009.

[46] G. Wagenknecht, H. Kaiser, F. Mottaghy, and H. Herzog, "MRI for attenuation correction in PET: methods and challenges," *Magnetic Resonance Materials in Physics*, vol. 26, no. 11, pp. 99–113, 2013.

[47] C. Berger, G. Goerres, S. Shoenes, A. Buck, A. Lonn, and G. C. Schulthess, "PET attenuation coefficients from CT images: experimental evaluation of the transformation of CT into PET 511-keV attenuation coefficients," *Eur J Nucl Med Mol Imaging*, vol. 29, no. 7, pp. 922–927, 2002.

[48] A. Attarwala, F. Molina-Duran, K. Büsing, S. Schönberg, D. Bailey, K. Willowson, and G. Glatting, "Quantitative and qualitative assessment of yttrium-90 PET/CT imaging," *PLoSONE*, vol. 9, no. 11, pp. 1–7, 2014.

[49] G. Delso, S. Fürst, B. Jakoby, R. Ladebeck, C. Ganter, S. Nekolla, M. Schwaiger, and S. Ziegler, "Performance measurements of the Siemens mMR integrated whole-body PET/MR scanner," *J Nucl Med*, vol. 52, no. 12, pp. 1914–22, 2011.

[50] B. Jakoby, Y. Bercier, C. Watson, B. Bendriem, and D. Townsend, "Performance characteristics of a new LSO PET/CT scanner with extended axial field-of-view and PSF reconstruction," *IEEE Transactions on Nuclear Science*, vol. 56, no. 3, pp. 633–639, 2009.

[51] J. Karp, S. Suleman, M. Daube-Withershpoon, and G. Muehllehner, "The benefit of time-of-flight in PET imaging: Experimental and clinical results," *J Nucl Med*, vol. 49, no. 3, pp. 462–470, 2008.

[52] K. Thielemans, E. Asma, S. Ahn, R. Manjeshwar, T. Deller, S. Ross, C. Stearns, and A. Ganin, "Impact of PSF modeling on the convergence rate and edge behavious of EM images in PET," *Nuclear Science Symposium Conference Record (IEEE NSS/MIC)*, pp. 3267–3272, 2010.

[53] C. Jaskowiak, J. Bianco, S. Perlman, and J. Fine, "Influence of reconstruction iterations on ^{18}F-FDG PET/CT standardized uptake values," *J Nucl Med*, vol. 46, no. 3, pp. 424–428, 2005.

[54] M. Brambilla, B. Cannillo, M. Dominietto, L. Leva, C. Secco, and E. Inglese, "Characterization of ordered subsets expectation maximization with 3D post-reconstruction Gauss filtering and comparison with filtered backprojection in ^{99m}Tc SPECT," *Annals of Nuclear Medicine*, vol. 19, no. 2, pp. 75–82, 2005.

[55] R. Boellaard, A. van Lingen, and A. Lammertsma, "Experimental and clinical evaluation of iterative reconstruction (OSEM) in dynamic PET: Quantitative characteristics and effects on kinetic modeling," *J Nucl Med*, vol. 42, no. 5, pp. 808–817, 2001.

[56] R. Boellaard, M. Hofman, O. Hoekstra, and A. Lammertsma, "Accurate PET/MR quantification using time of flight MLAA in image reconstruction," *Mol Imaging Biol*, vol. 16, no. 4, pp. 469–77, 2014.

[57] J. Kim, J. Lee, I. Song, and D. Lee, "Comparison of segmentation-based attenuation methods for PET/MRI: Evaluation of bone and liver standardized uptake value with oncologic PET/CT data," *J Nucl Med*, vol. 53, no. 12, pp. 1878–1882, 2012.

[58] D. Izquierdo-Garcia, S. Sawiak, K. Knesaurek, J. Narula, V. Fuster, J. Machac, and Z. Fayad, "Comparison of MR-based attenuation correction vs. CT-based attenuation correction of whole body PET/MR imaging," *Eur J Nucl Med Mol Imaging*, vol. 41, no. 8, pp. 1574–1584, 2014.

[59] M. Eiber, A. Martinez-Möller, M. Souvatzoglou, K. Holzapfel, A. Pickhard, D. Löffelbein, I. Santi, E. Rummeny, S. Ziefler, M. Schwaiger, S. Nekolla, and A. Beer, "Value of a Dixon-based MR/PET attenuation correction sequence for the localization and evaluation of PET-positive lesions," *Eur J Nucl Med Mol Imaging*, vol. 38, no. 9, pp. 1691–701, 2011.

[60] J. Lau, R. Laforest, H. Sotoudeh, X. Nie, S. Sharma, J. McConathy, E. Novak, A. Priatna, R. Gropler, and P. Woodard, "Evaluation of attenuation correction in cardiac PET using PET/MR," *J Nucl Cardiology*, p. online first, 23 Oct 2015.

[61] F. Fahey, P. Kinahan, R. Doot, M. Kocak, H. Thurston, and T. Poussaint, "Variability in PET quantification within a multicenter consortium," *Med Phys*, vol. 37, no. 7, pp. 3660–3666, 2010.

[62] M. Elschot, B. Vermolen, M. Lam, B. de Keizer, M. van den Bosch, and H. de Jong, "Quantitative comparison of PET and bremsstrahlung SPECT for imaging the in vivo yttrium-90 microsphere distribution after liver radioembolization," *PLoS ONE*, vol. 8, no. 2, p. e55742, 2013.

[63] R. Lhommel, L. van Elmbt, G. Pierre, M. van den Eynde, J. François, S. Pauwels, and S. Walrand, "Feasibility of 90Y TOF PET-based dosimetry in liver metastasis therapy using SIR-Spheres," *EJNMMI*, vol. 37, no. 9, pp. 1654–1662, 2010.

[64] A. van den Hoven, C. Rosenbaum, S. Elias, H. de Jong, M. Kiipman, H. Verkooijen, A. Alavi, M. van den Bosch, and M. Lam, "Insights into the dose-response relationship of radioembolization with resin 90Y-microspheres: a prospective cohort study in patients with colorectal cancer liver metastases," *J Nucl Med*, vol. 57, no. 7, pp. 1014–9, 2016.

[65] X. Liu, C. Comtat, C. Michel, P. Kinahan, M. Defrise, and D. Townsend, "Comparison of 3-D reconstruction with 3D-OSEM and with FORE+OSEM for PET," *IEEE Transactions on Medical Imaging*, vol. 20, no. 8, pp. 804–814, 2001.

[66] L. Grezes-Besset, J. Nuyts, and R. Boellard, "Simulation-based evaluation of NEG-ML iterative reconstruction of low count PET data.," *2007 IEEE Nuclear Science Symposium Conference Record*, pp. 3009–14, 2007.

[67] F. van Velden, R. Kloet, B. van Berckel, A. Lammertsma, and R. Boellaard, "Accuracy of 3-dimensional reconstruction algorithms for the high-resolution research tomograph," *J Nucl Med*, vol. 50, no. 1, pp. 72–80, 2009.

[68] J. Qi, R. Leahy, C. Hsu, T. Farquhar, and S. Cherry, "Fully 3D Bayesian image reconstruction for the ECAT EXACT HR+," *IEEE Transactions on Nuclear Science*, vol. 45, no. 3, pp. 1096–1103, 1998.

[69] S. Vandenberghe, E. Mikhaylova, E. D'Hoe, P. Mollet, and J. Karp, "Recent developments in time-of-flight PET," *Eur J Nucl Med Mol Imaging*, vol. 3, no. 3, p. 16 Feb 2016, 2016.

[70] K. Fowler, N. Maughan, R. Laforest, N. Saad, A. Sharma, J. Olsen, C. Speirs, and P. Parikh, "PET/MRI of hepatic 90Y microsphere deposition determines individual tumor response," *Cardiovascular and Interventional Radiology*, vol. 39, no. 6, pp. 855–64, 2016.

[71] W. Bolch, L. Bouchet, and J. R. et al, "MIRD pamphlet No 17: the dosimetry of nonuniform activity distributions–radionuclide S values at the voxel level," *Medical Internal Radiation Dose Committee, J Nucl Med*, vol. 40, no. 1, pp. 11S–36S, 1999.

[72] W. Lea, K. Tapp, and M. T. et al, "Microsphere localization and dose quantification using positron emission tomography/CT following hepatic intraarterial radioembolization

with Yttrium-90 in patients with advanced hepatocellular carcinoma," *J Vasc Interv Radiol*, vol. 25, pp. 1595–1603, 2014.

[73] E. Eisenhauer, P. Therasse, J. Bogaerts, L. Schwartz, D. Sargent, R. Ford, J. Dancey, S. Arbuck, S. Gwyther, M. Mooney, L. Rubstein, L. Shankar, L. Dodd, R. Kaplan, D. Lacombe, and J. Verweij, "New response evaluation criteria in solid tumours: revised recist guideline (version 1.1)," *Eur J Cancer*, vol. 45, no. 2, pp. 228–47, 2009.

[74] M. D'Arienzo, P. Chiaramida, and L. C. et al, "90Y PET-based dosimetry after selective internal radiotherapy treatments," *Nucl Med Commun*, vol. 33, no. 6, pp. 633–40, 2012.

[75] A. Gupta, A. Gill, S. Shrikanthan, and S. Srinivas, "Nontargeted Y-90 microsphere radioembolization to duodenum visualized on Y-90 PET/CT ond Bremsstrahlung SPECT/CT," *Clin Nucl Med*, vol. 37, no. 1, pp. 98–9, 2012.

[76] V. Tacher, M. Lin, R. Duran, H. Yarmohammadi, H. Lee, J. Chapiro, M. Chao, Z. Wang, C. Frangakis, J. Sohn, M. Maltenfort, T. Pawlik, and J. Geshwind, "Comparison of existing response criteria in patients with hepatocellular carcinoma treated with transarterial chemoembolization using a 3D quantitative approach," *Radiology*, vol. 278, no. 1, pp. 275–84, 2016.

[77] S. Padia, A. Alessio, and S. K. et al, "Comparison of positron emission tomography and bremsstrahlung imaging to detect particle distribution in patients undergoing yttrium-90 radioembolization for large hepatocellular carcinomas or associated portal vein thrombosis," *J Vasc Interv Radiol*, vol. 24, no. 8, pp. 1147–53, 2013.

[78] S. Srinivas, N. Natarajan, and J. K. et al, "Determination of radiation absorbed dose to primary liver tumors and normal liver tissue using post-radioembolization 90Y PET," *Frontiers in Oncology*, vol. 4, p. article 255, 2014.

[79] T. Chang, A. Bourgeois, and A. B. et al, "Treatment modification of yttrium-90 radioembolization based on quantitative positron emission tomorgraphy/CT imaging," *J Vasc Interv Radiol*, vol. 24, no. 3, pp. 333–7, 2013.

[80] Y. Petibon, C. Huang, J. Ouyang, T. Reese, Q. Li, A. Syrking, Y. Chen, and G. El Farhri, "Relative role of motion and PSF compensation in whole-body oncologic PET-MR imaging," *Med Phys*, vol. 41, no. 4, p. 042503, 2014.

[81] H. Ahmadzadehfar, A. Sabet, K. Biermann, M. Muckle, H. Brockmann, C. Kuhl, K. Wilhelm, H. Biersack, and S. Ezziddin, "The significance of 99mTc-MAA SPECT/CT liver perfusion imaging in treatment planning for 90Y-microsphere selective internal radiation treatment," *J Nucl Med*, vol. 51, no. 8, pp. 1206–1212, 2010.

[82] P. Flamen, B. Vanderlinden, P. Delatte, G. Ghanem, L. Ameye, M. Van Den Eynde, and A. Hendlisz, "Multimodality imaging can predict the metabolic response of unresectable

colorectal liver metastases to radioembolization therapy with Yttrium-90 labeled resin microspheres," *Phys. Med. Biol.*, vol. 53, pp. 6591–6603, 2008.

[83] E. Garin, L. Lenoir, Y. Rolland, J. Edeline, H. Mesba, and S. L. et al, "Dosimetry based on 99mTc-macroaggregated albumin SPECT/CT accurately predicts tumor response and survival in hepatocellular carcinoma patients treated with 90Y-loaded glass microspheres: preliminary results," *J Nucl Med.*, vol. 53, no. 2, pp. 255–63, 2012.

[84] M. Lam, M. Goris, A. Iagaru, E. Mittra, J. Louie, and D. Sze, "Prognostic utility of 90Y radioembolization dosimetry based on fusion 99mTc-macroaggregated albumin-99mTc-sulfur colloid SPECT," *J Nucl Med*, vol. 54, no. 12, pp. 2055–61, 2013.

[85] Y. Song, J. Paeng, H. Kim, J. Chung, G. Cheon, J. Chung, D. Lee, and K. Kang, "PET/CT-based dosimetry in 90Y-microsphere selective internal radiation therapy: Single cohort comparison with pretreatment planning on 99mTc-MAA imaging and correlation with treatment efficacy," *Medicine*, vol. 94, no. 23, p. e945, 2015.

[86] P. Parikh, N. Maughan, A. Weiner, K. Fowler, R. LaForest, and N. Saad, "Clinical impact of PET/MRI dosimetry after radioembolization," *Eur Assoc Nucl Med Annual Meeting*, p. EPR132, 2016.

[87] E. Garin, Y. Rolland, S. Laffont, and J. Edeline, "Clinical impact of 99mTc-MAA SPECT/CT-based dosimetry in the radioembolization of liver malignances with 90Y-loaded microspheres," *Eur J Nucl Med Mol Imaging*, vol. 43, pp. 559–575, 2016.

[88] S. Ho, W. Lau, T. Leung, M. Chan, Y. Ngar, P. Johnson, and A. Li, "Partition model for estimating radiation doses from yttrium-90 microspheres in treating hepatic tumours," *Eur J Nucl Med*, vol. 23, no. 8, pp. 947–52, 1996.

[89] E. Garin, Y. Rolland, J. Edeline, N. Icard, L. Lenoir, S. Laffont, H. Mesbah, M. Breton, L. Sulpice, K. Boudjema, R. Rohou, J. Raoul, B. Clement, and E. Boucher, "Personalized dosimetry and intensification concept with 90Y-loaded glass microsphere radioembolization induce prolonged overall survival in hepatocellular carcinoma patients with portal vein thrombosis," *J Nucl Med*, vol. 56, no. 3, pp. 339–46, 2015.

[90] K. Knesaurek, J. Machac, M. Muzinic, M. DaCosta, Z. Zhang, and S. H. S, "Quantitative comparison of yttrium-90 (90Y)-microspheres and technetium-99m (99mTc)-macroaggregated albumin SPECT images for planning 90Y therapy of liver cancer," *Technol Cancer Res Treat*, vol. 9, no. 3, pp. 253–62, 2010.

[91] M. Wondergem, M. Smits, M. Elschot, H. de Jong, H. Verkooijen, and M. v. et al, "99mTc-macroaggregated albumin poorly predicts the intrahepatic distribution of 90Y resin microspheres in hepatic radioembolization," *J Nucl Med*, vol. 54, no. 8, pp. 1294–301, 2013.

[92] A. Dhabuwala, P. Lamerton, and R. Stubbs, "Relationship of 99m-technetium labelled macroaggregated albumin (99mTcMAA) uptake by colorectal liver metastases to response following selective internal radiation therapy (SIRT)," *BMC Nucl Med*, vol. 5, p. 7, 2005.

[93] G. Ulrich, O. Dudeck, C. Furth, J. Ruf, O. Grosser, D. Adolf, M. Stiebler, J. Ricke, and H. Amthauer, "Predictive value of intratumoral 99mTc-macroaggregated albumin uptake in patients with colorectal liver metastases scheduled for radioembolization with 90Y-microspheres," *J Nucl Med*, vol. 54, no. 4, pp. 516–22, 2013.

[94] C. Van de Wiele, A. Maes, E. Brugman, Y. DAsseler, B. De Spiegeleer, and G. M. et al, "SIRT of liver metastases: physiological and pathophysiological considerations," *Eur J Nucl Med Mol Imaging*, vol. 39, no. 10, pp. 1649–55, 2012.

[95] E. Garin, L. Lenoir, J. Edeline, S. Laffont, H. Mesbah, and P. P. et al, "Boosted selective internal radiation therapy with 90Y-loaded glass microspheres (B-SIRT) for hepatocellular carcinoma patients: a new personalized promising concept," *Eur J Nucl Med Mol Imaging*, vol. 40, no. 7, pp. 1057–68, 2013.

[96] G. El Fakhri, I. Buvat, H. Benali, A. Todd-Pokropek, and R. Di Paolo, "Relative imparct of scatter, collimator response, attenuation, and finite spatial resolution corrections in cardiac SPECT," *J Nucl Med*, vol. 41, no. 8, pp. 1400–8, 2000.

Curriculum Vitae

Nichole Millward Maughan

Degrees

Washington University, St. Louis, MO
Ph.D. Biomedical Engineering   May 2017
M.S. Biomedical Engineering   December 2016

Brigham Young University, Provo, UT
M.S. Physics   June 2013
B.S. Physics   August 2011
Mathematics Minor

Professional Societies

Society of Nuclear Medicine and Molecular Imaging
Institute of Electrical and Electronic Engineers
Society of Interventional Radiology
International Society of Magnetic Resonance in Medicine

Publications

*NM Maughan, *KJ Fowler, R Laforest, NE Saad, A Sharma, J Olsen, CK Speirs, PJ Parikh. PET/MRI of Hepatic 90Y microsphere deposition: determining dose response correlation, Cardiovascular and Interventional Radiology. 39(6); 2016: 855-64. *co-first authors.

NM Maughan, M Eldib, M Conti, K Kneaurek, D Faul, ZA Fayad, PJ Parikh, R Laforest. Phantom Study to Determine Optimal PET Reconstruction Parameters for PET/MR Imaging of 90Y Microspheres Following Radioembolization, Biomedical Physics and Engineering Express. 2(1); 2016: 015009.

L Rankine, H Wan, P Parikh, **NM Maughan**, P Poulsen, T DeWees, E Klein, L Santanam. Cone-Beam Computed Tomography (CB-CT) internal motion tracking

should be used to validate 4-Dimensional CT for abdominal radiotherapy patients, Journal of Radiation Oncology, Biology, and Physics. 95(2); 2016: 818-26.

NM Maughan, JW Moody, DR Miller. Monte Carlo simulation of near-infrared light propagation through homogeneous mixed media, Journal of Biomedical Optics. 18(10); 2013.

Proceedings

NM Maughan, M Eldib, D Faul, R Laforest, M Conti, M Elschot, K Knesaurek, FA Leek, DW Townsend, FP DiFilippo, KK Jackson, M Tapner, PJ Parikh. "Multi-institutional phantom study of yttrium-90 PET-based dosimetry of hepatic radioembolization using PET/MRI: The MR-QUEST Study." Oral presentation at SNMMI Annual Meeting, June 2017, Denver, CO.

NM Maughan, J Garcia-Ramirez, M Arpidone, A Swallen, R Laforest, SM Goddu, PJ Parikh, J Zoberi. "Commissioning of Post-Treatment PET-Based Dosimetry Software for Hepatic Radioembolization of Yttrium-90 Microspheres." Oral presentation at American Brachytherapy Society Annual Meeting, April 2017, Boston, MA.

NM Maughan, PJ Parikh, R Laforest. "Low Trues Statistics and High Randoms Rates Degrade Quantitative Accuracy in PET Iterative Reconstruction Methods." Poster presentation at IEEE Nuclear Science Symposium and Medical Imaging Conference, November 2016, Strasbourg, France.

NM Maughan. "Imaging, Software, and Workflow for Quantitative Dosimetry of Yttrium-90 Radioembolization." Invited oral presentation at MIM Software Users Meeting at European Association of Nuclear Medicine Annual Meeting, October 2016, Barcelona, Spain.

NM Maughan, KJ Fowler, R Laforest, A Sharma, J Olsen, CK Speirs, T DeWees, PJ Parikh, NE Saad. "Correlation between Pre-Treatment 99mTc-MAA SPECT and Post-Radioembolization 90Y PET." Oral presentation at European Association of Nuclear Medicine Annual Meeting, October 2016, Barcelona, Spain.

PJ Parikh, **NM Maughan**, A Weiner, K Fowler, R Laforest, N Saad. "Clinical Impact of PET/MRI Dosimetry after Radioembolization." E-poster presentation at European Association of Nuclear Medicine Annual Meeting, October 2016, Barcelona, Spain.

NM Maughan, D Muccigrosso, H Schultejans, R Bera, PJ Parikh. "Continuous Tracking of Lung Tumor Motion at 3.3 Hz or Faster is Necessary to Accurately Represent Motion." Poster presentation at ASTRO Annual Meeting, September 2016, Boston, MA.

D Muccigrosso, **NM Maughan**n, H Wan, Y Lu, H Schultejans, R Bera, PJ Parikh. "The relationship between implantation distance and fraction number with fiducial accuracy during lung cancer radiation therapy." Poster presentation at ASTRO Annual Meeting, September 2016, Boston, MA.

K Grantham, H Wan, **NM Maughan**, D Muccigrosso, H Schultejans, R Bera, PJ Parikh. "Stability of mean lung tumor position over the course of radiation therapy as measured by continuous electromagnetic transponder tracking." Poster Presentation at ASTRO Annual Meeting, September 2016, Boston, MA.

D Muccigrosso, **NM Maughan**, H Schultejans, R Bera, PJ Parikh. "Correlation of Lung Tumor Motion with Tumor Location Using Electromagnetic Tracking." Poster Presentation at AAPM Annual Meeting, August 2016, Washington, D.C.

N Saad, K Fowler, **NM Maughan**, R Laforest, A Sharma, C Speirs, J Olsen, P Parikh. "PET/MRI of hepatic 90Y microsphere deposition determines individual tumor response." Oral Presentation at Society of Interventional Radiology Annual Scientific Meeting, April 2016, Vancouver, B.C., Canada.

NM Maughan, M Eldib, M Conti, K Kneaurek, D Faul, ZA Fayad, PJ Parikh, R Laforest. "Phantom Study to Determine Optimal PET Reconstruction Parameters for PET/MR Imaging of 90Y Microspheres Following Radioembolization." Poster presentation at IEEE Nuclear Science Symposium and Medical Imaging Conference, November 2015, San Diego, CA.

NM Maughan, KJ Fowler, R Laforest, NE Saad, A Sharma, J Olsen, CK Speirs, PJ Parikh. "Y-90 PET/MRI Predicts Treatment Response after Hepatic Radioembolization." Oral presentation in Physics Scientific Session at ASTRO Annual Meeting, October 2015, San Antonio, TX.

LJ Rankine, H Wan, PJ Parikh, **NM Maughan**, PR Poulsen, L Santanam. "Cone Beam CT Measures Abdominal Tumor Motion Better than 4DCT and Equal to On-table Fluoroscopy." Oral Presentation at ASTRO Annual Meeting, October 2015, San Antonio, TX.

NM Maughan, M Conti, PJ Parikh, D Faul, R Laforest. "Phantom Study to Determine Optimal PET Reconstruction Parameters for PET/MR Imaging of Y-90 Microspheres Following Radioembolization." SNAP Oral Presentation at AAPM Annual Meeting, July 2015, Anaheim, CA.

NM Maughan, KJ Fowler, R Laforest, NE Saad, A Sharma, J Olsen, CK Speirs, PJ Parikh. "Using PET/MRI to Assess Radioembolization of Y-90 Microspheres." Poster presentation at ISMRM Motion Correction Workshop, July 2014, Troms, Norway.

NM Maughan, DR Miller, JW Moody. "Simulation of Mid-IR Light Propagation Through the Human Finger for Non-Invasive Blood Analysis." Oral presentation at BYU College of Physical and Mathematical Sciences Student Spring Research Conference, March 2012.

NM Maughan, S Norman, BJ Campbell. "Defect-Induced Diffuse Scattering in Microporous Aluminophosphate-5." Oral presentation at BYU College of Physical and Mathematical Sciences Student Spring Research Conference, March 2012.

NM Maughan, S Norman, BJ Campbell. "Framework defects in microporous materials." Oral presentation at American Physical Society Four Corners Annual Meeting, October 2011.

May 2017

PET/MRI Dosimetry of Yttrium-90 Radioembolization, Maughan, Ph.D. 2017